

Water Resources Research®

RESEARCH ARTICLE

10.1029/2023WR036450

Special Collection:

Hydrogeodesy: Understanding changes in water resources using space geodetic observations

Key Points:

- A new methodology for integrating synthetic aperture radar backscattering coefficients with optical remote sensing-based inland surface water dynamics is developed
- Monthly inundated area and water storage changes of 721 large reservoirs in China during 2017–2021 are retrieved at improved accuracy
- Impacts of natural climate and human control on the inter- and intra-annual variations in reservoir water across different regions in China are analyzed

Supporting Information:

Supporting Information may be found in the online version of this article.

Correspondence to:

D. Long,
dlong@tsinghua.edu.cn

Citation:

Chen, Y., Wang, Y., Li, L., Cui, Y., Duan, X., & Long, D. (2024). Monthly monitoring of inundated areas and water storage dynamics in China's large reservoirs using multisource remote sensing. *Water Resources Research*, 60, e2023WR036450. <https://doi.org/10.1029/2023WR036450>

Received 7 OCT 2023

Accepted 29 JUL 2024

Author Contributions:

Conceptualization: Yongzhe Chen, Di Long

Data curation: Yongzhe Chen

Formal analysis: Yongzhe Chen

Funding acquisition: Di Long

Investigation: Yongzhe Chen,

Yiming Wang, Luoqi Li




Methodology: Yongzhe Chen,

Yiming Wang

© 2024. The Author(s).

This is an open access article under the terms of the [Creative Commons Attribution License](https://creativecommons.org/licenses/by/4.0/), which permits use, distribution and reproduction in any medium, provided the original work is properly cited.

Monthly Monitoring of Inundated Areas and Water Storage Dynamics in China's Large Reservoirs Using Multisource Remote Sensing

Yongzhe Chen^{1,2} , Yiming Wang^{1,2}, Luoqi Li^{1,2}, Yanhong Cui^{1,2}, Xingwu Duan^{3,4} , and Di Long^{1,2,4} 

¹Department of Hydraulic Engineering, Tsinghua University, Beijing, China, ²Key Laboratory of Hydrosphere Sciences of the Ministry of Water Resources, Tsinghua University, Beijing, China, ³Institute of International Rivers and Eco-security, Yunnan University, Kunming, China, ⁴Southwest United Graduate School, Kunming, China

Abstract High-frequency monitoring of reservoir inundation and water storage changes is crucial for reservoir functionality assessment and hydrological model calibration. Although the integration of optical data with synthetic aperture radar (SAR) backscattering coefficients (backscatters) offers an effective approach, conventional methods struggle to consistently provide accurate retrievals over diverse regions and seasons. In this study, we introduce reservoir- and monthly-specific classification models to enhance the integration of Sentinel-1 SAR backscatters with optical-based water dynamics. Our method covers 721 reservoirs with a capacity greater than 0.1 km³ in China during 2017–2021. Furthermore, we leverage multisource satellite altimetry records (e.g., ICESat-2, CryoSat-2, and GEDI) and digital elevation models to derive hypsometry relationship (i.e., water level–water area relationship) for reservoirs, enabling the transformation of inundated areas into monthly water storage changes for 662 reservoirs, representing 93% of the total storage capacity of large reservoirs. Validation against in-situ measurements at 80 reservoirs reveals improved monthly inundated area monitoring compared to existing data sets. Additionally, our reservoir water storage change estimates exhibit an average R^2 of 0.79 and a mean relative root mean square error (rRMSE) of 21%. Our findings highlight reservoir water increases from May/June to November and declines in winter–spring in most regions. However, the inter-annual patterns vary among regions, with increases in Northeast China, the Yellow River basin (YR), and Southwest China, contrasted by declines in Eastern and Northwest China. Inter- and intra-annual variability in reservoir water storage is mainly influenced by natural inflow in Northeast and Northwest China, while anthropogenic factors dominate in the YR, Eastern, and Southwest China.

Plain Language Summary Reservoirs can supply water, control flood and provide electricity. Without high temporal frequency data on inundated area and water storage over a large spatial extent, we could not clearly understand how and to which degree numerous reservoirs have altered the natural water cycle and provided multiple benefits to people all across the world. The development of remote sensing technology has facilitated the long-term monitoring of inundated areas and water levels of large quantities of reservoirs. However, high-temporal-resolution monitoring remains challenging. In this study, by developing a novel method which integrates active microwave remote sensing data with optical remote sensing observations, we largely improved the satellite-based monthly inundated area and water storage change monitoring at almost all large reservoirs in China. The results reveal distinct seasonal patterns and interannual variations of reservoir water in different regions of China. Specifically, we found that reservoirs in Northeast China, the Yellow River basin, and Southwest China generally expanded, whereas those in Eastern and Northwest China generally shrank during 2017–2021. The climatic and anthropogenic impacts on the inter- and intra-annual variations in reservoir water across different regions were also analyzed.

1. Introduction

Over the past six decades, humanity has witnessed an unprecedented surge in reservoir construction, reshaping landscapes and hydrological dynamics worldwide (Lehner et al., 2011; Mulligan et al., 2020). Globally, more than 7,320 large reservoirs with a storage capacity exceeding 0.1 km³ (Lehner et al., 2019), serve multiple purposes, from irrigation and water supply to flood control, aquaculture, hydropower generation, and navigation (Intralawan et al., 2018). Notably, China, steeped in a rich history of reservoir development, has built over 90,000 reservoirs since 1954, representing approximately 40% of the world's largest dams (Song et al., 2022). However,

Project administration: Di Long
Resources: Di Long
Supervision: Di Long
Validation: Yongzhe Chen
Writing – original draft: Yongzhe Chen
Writing – review & editing:
 Yiming Wang, Luoqi Li, Yanhong Cui,
 Xingwu Duan, Di Long

this prolific growth in dam infrastructure has substantially altered the natural flow of rivers, challenging ecosystems and hydrological balance (Gou et al., 2021; Grill et al., 2019; Han et al., 2020; Zhu et al., 2020).

While hydrological models can simulate natural runoff patterns (Gou et al., 2021), they face significant limitations when addressing actual river discharge in regions with sparse information on reservoir water levels and storage changes. This scarcity hampers the accurate simulation of river flow under the influence of human-managed reservoirs, where traditional models often struggle to integrate complex reservoir operation rules (Biemans et al., 2011; Dong et al., 2022; Han et al., 2020). To bridge this gap, satellite observations, encompassing frozen areas within reservoirs and frequent monitoring of water storage dynamics, offer a vital tool for calibrating and refining hydrological models under human-managed scenarios (Han et al., 2020).

Furthermore, high-frequency monitoring of inundated areas and water storage changes emerges as a powerful strategy for evaluating the multifaceted functionality of reservoirs, estimating evaporative and seepage losses (G. Zhao et al., 2022), and assessing ecological health and greenhouse gas emissions in littoral zones and drawdown areas (Keller et al., 2021; Soued et al., 2022; Yuan et al., 2013). To date, optical remote sensing stands out as the primary tool for capturing inter-annual dynamics in inundated areas (Pekel et al., 2016; Pickens et al., 2020). However, the persistent challenge of cloud contamination limits its effectiveness in providing high-frequency data, particularly on a monthly basis. Monthly surface water maps derived from optical imagery, such as those developed by the Joint Research Center (JRC) and the Global Land Analysis and Discovery (GLAD) group (Pekel et al., 2016; Pickens et al., 2020), often contain large areas without information (Figure S1 in Supporting Information S1). While efforts have been made to overcome these limitations, some reservoirs still suffer from data gaps during cloudy or frozen months (G. Zhao & Gao, 2018; G. Zhao et al., 2022).

An alternative approach to high-frequency surface water mapping is the utilization of synthetic aperture radar (SAR) images. Microwave signals can penetrate clouds, and SAR backscatters from water and seasonally frozen water are typically lower than those from surrounding land areas (Y. Li et al., 2020). However, inherent noise in SAR images and the incidence angle effect (Figures S2a and S2b in Supporting Information S1) contribute to lower accuracy in surface water identification compared to optical remote sensing (Feng et al., 2021; Y. Li et al., 2020). In addition, freezing and snowpack can increase SAR backscatters of water bodies, while lands with limited vegetation cover and soil moisture, such as sand dunes and mudflats could have very low SAR backscatters, similar to surface water. Therefore, in relatively arid regions and during cold seasons, SAR backscatters of some water bodies can be similar to or even higher than the surrounding land, yet some other nearby water bodies have lower SAR backscatters than their surrounding land (Figures S2c and S2d in Supporting Information S1). These complexities render the Otsu or local thresholding method, which identifies pixels with SAR backscatter values lower than an estimated regional threshold as surface water (Bonnema et al., 2022; Liang & Liu, 2020; Otsu, 1979), unsuitable for all reservoirs and seasons. Although recent studies have turned to local thresholding approaches and the integration of SAR backscatters with optical imagery through regional adaptive machine learning models (Druce et al., 2021; Hird et al., 2017; Konapala et al., 2021; Liang & Liu, 2020; Tang et al., 2022; Y. Wang et al., 2023). These approaches may have overlooked spatial variations in threshold backscatter values within the same region, as well as temporal variations in threshold values caused by seasonal changes in SAR backscatters of surface waters and surrounding terrain (Z. Jiang et al., 2021; Souza et al., 2022). Consequently, the quality of reservoir inundated area monitoring, particularly in regions with frozen water bodies, remains a challenge, necessitating more efforts for improvement.

Accurate estimation of water levels is vital for determining water storage changes (X. Li et al., 2019). While satellite altimetry data obtained through radar and LiDAR altimeters are valuable, its coverage is often insufficient for most reservoirs (Cooley et al., 2021; Hou et al., 2022; Shen et al., 2022). To derive water levels in many reservoirs, inundated areas are often combined with digital elevation model (DEM)-based reservoir hypsometry relationship, which is the relationship between water level and inundated area (Hou et al., 2022). Hypsometry relationship curves are well-fitted when DEM data above the lowest water level of the reservoir are readily available (Avisse et al., 2017). In the absence of such data, a lower accuracy estimation of the mean depth of each water body and subsequent hypsometry relationship can be obtained by extrapolating surrounding topography through a geostatistical model (Khazaei et al., 2022; Messenger et al., 2016). While satellite altimetry data offer enhanced accuracy compared to DEMs (Magruder et al., 2021), further integration of high-quality satellite altimetry records and diverse DEM sources is still required to improve the robustness of hypsometry relationship estimation.

Given the strengths and limitations inherent in existing methodologies (limited temporal frequency, spatial coverage, or data quality), this study aims to achieve high-quality monthly monitoring of inundated areas and water storage changes for almost all large reservoirs with total storage exceeding 0.1 km^3 across China. This will be accomplished by enhancing the integration of multisource remote sensing data, including optical remote sensing, SAR imagery, radar, LiDAR altimetry, and diverse DEMs. For example, to improve monitoring reservoir inundated areas, this study developed reservoir- and monthly-specific supervised classification models, and applied the optical remote sensing-based surface water identification results as the training samples. Ultimately, our study seeks to unveil inter- and intra-annual variations in reservoir inundated areas and water storage across different regions of China, while exploring potential drivers of these changes. The findings will provide essential insights for assessing reservoir performance, estimating losses due to evaporation and seepage, and calibrating hydrological models.

2. Data and Preprocessing

2.1. Surface Water Dynamics Data Sets Derived From Optical Imagery

Both the JRC and the GLAD group have mapped annual permanent and seasonal surface water at a 30-m resolution using Landsat data (see Figure S1 in Supporting Information S1 for examples of images). The JRC data set spans from 1984 to 2021, while the GLAD data set covers the years 1999–2021 (Pekel et al., 2016; Pickens et al., 2020). These global surface water dynamics data sets, based on optical remote sensing, offer insights into surface water distribution on an annual and monthly basis. However, the monthly maps are susceptible to missing values, primarily due to factors such as low solar elevation angles, cloud contamination, and snow or ice cover. To address this challenge, our study leveraged these optical remote sensing-based annual and monthly surface water maps to identify inundated and dry pixels within each reservoir for each month, a critical step detailed in Section 3.1. These identified pixels were subsequently utilized as training samples in our analysis.

2.2. A Calibrated Geospatial Data Set of All Large Reservoirs in China

The China Reservoir Data set (CRD) was created through the amalgamation of various global and national reservoir databases, bolstered by multisource open map data integration (Song et al., 2022). Initially, we identified 901 potentially large reservoirs within the CRD, defined either by their reported or estimated total storage exceeding 0.1 km^3 or classified as large reservoirs within the CRD itself. Subsequently, through cross-referencing with government reports, we identified 148 medium-sized reservoirs that had been misclassified as large reservoirs within the CRD. These were subsequently excluded from our analysis. Additionally, we incorporated the missing data of 32 large reservoirs that were omitted in the CRD.

To determine the maximum surface water extent during our study period from 2017 to 2021, we employed a combination of the JRC and GLAD products. By converting the raster data into shapefiles representing inland surface water bodies and utilizing Google Earth to identify the geographical locations of the missing large reservoirs within the CRD, we approximated the extents of these 32 large reservoirs. Through these efforts, we successfully generated a comprehensive geospatial data set comprising 785 large reservoirs located across China (Figure 2). Furthermore, we verified and corrected the information pertaining to the total storage capacity of each reservoir. The shapefiles of 785 large reservoirs were subsequently converted into a raster file whose spatial resolution and extent match those of the GLAD/JRC surface water percent maps.

China's diverse geographical landscape and reservoir functionality prompted us to partition the nation into five distinct regions, considering climatic variances and the primary functions of the large reservoirs examined in our study. These regions encompass Northeast China (NE), Eastern China (EA), the upper and middle reaches of the Yellow River basin (YR), Southwest China (SW), and Northwest China (NW) (Figure 1). Criteria governing the division of these regions and the predominant functions of reservoirs in each region are shown in Text S1 in Supporting Information S1.

2.3. Sentinel-1 SAR Data Preprocessing

The European Space Agency's (ESA) Sentinel-1 Earth Observation Mission comprises two satellites, namely Sentinel-1A and Sentinel-1B. Sentinel-1A was successfully launched in April 2014 and continues to operate properly. In contrast, Sentinel-1B, launched in April 2016, ceased operations in January 2022. During the period

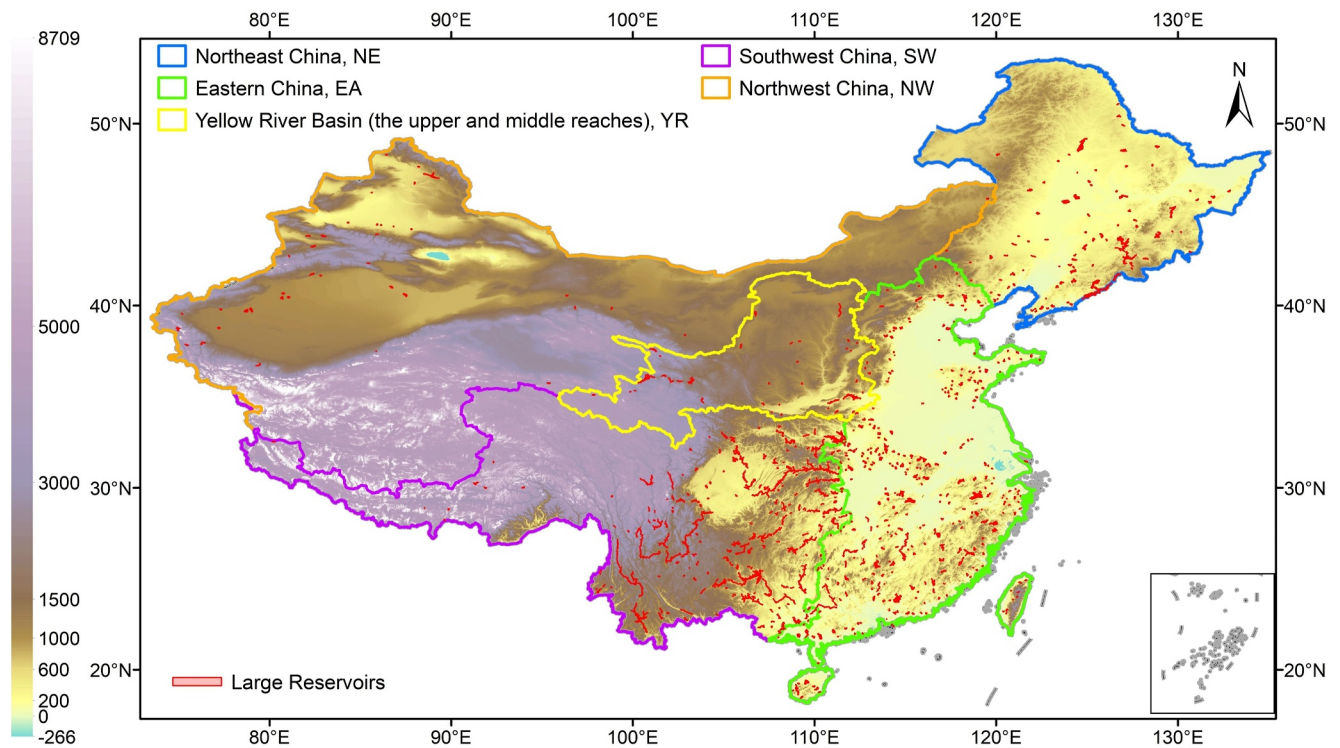


Figure 1. Spatial distribution of 785 large reservoirs in China examined in this study (background map shows Multi-Error-Removed Improved-Terrain-Digital Elevation Model).

spanning January 2017 to December 2021, both Sentinel-1A and Sentinel-1B consistently acquired high-quality C-band SAR images, resulting in an impressive observation frequency of four to five times per month. Consequently, we designated these 60 months as our study periods.

Vertical-vertical (VV) and vertical-horizontal polarized backscatters retrieved in the in the Interferometric Wideswath mode are readily available as Ground Range Detected images through the Google Earth Engine (GEE). These images have undergone a series of essential preprocessing steps, including thermal noise removal, radiometric calibration, and basic terrain correction. To further refine the calibration of these images, we executed border noise removal, mono-temporal Lee-Sigma speckle filtering (Lee et al., 2009), and radiometric terrain flattening (Mullissa et al., 2021; Vollrath et al., 2020). After all these calibrations, the radar backscatter can be provided as gamma-naught (γ^0), which has been recommended compared to the conventional sigma-naught (Small, 2011).

After the normalization process, the co-polarized backscatters exhibit less disturbance from variations in incidence angle (Shamshiri et al., 2022). In contrast, cross-polarized backscatters still show significant variations with changing incidence angles, often resulting in disruptive stripes within the imagery (Feng et al., 2021; Shamshiri et al., 2022). Consequently, we exclusively relied on VV-polarized backscatters for our inundated probability predictions. Since wind or rainfall-roughened water surfaces can be dominated by surface scattering instead of specular reflection, leading to elevated backscatters comparable to those from land areas (S. Li et al., 2018), we should exclude SAR observations on potential windy days to better distinguish between water and land areas (Gulácsi & Kovács, 2020). Thus, for each pixel, encompassing both water and land, we computed the lower quantiles (25%) of all VV backscatters in a month. Considering there are typically four to five Sentinel-1 observations per month, the lowest quantiles represent either the lowest or the average between the lowest and the second lowest retrievals for each month. Examples of monthly composites of the processed VV-polarized backscatters (γ^0) in China are shown in Figure S2 in Supporting Information S1. These monthly composites were resampled to 30 m resolution to align with the resolution of JRC and GLAD data.

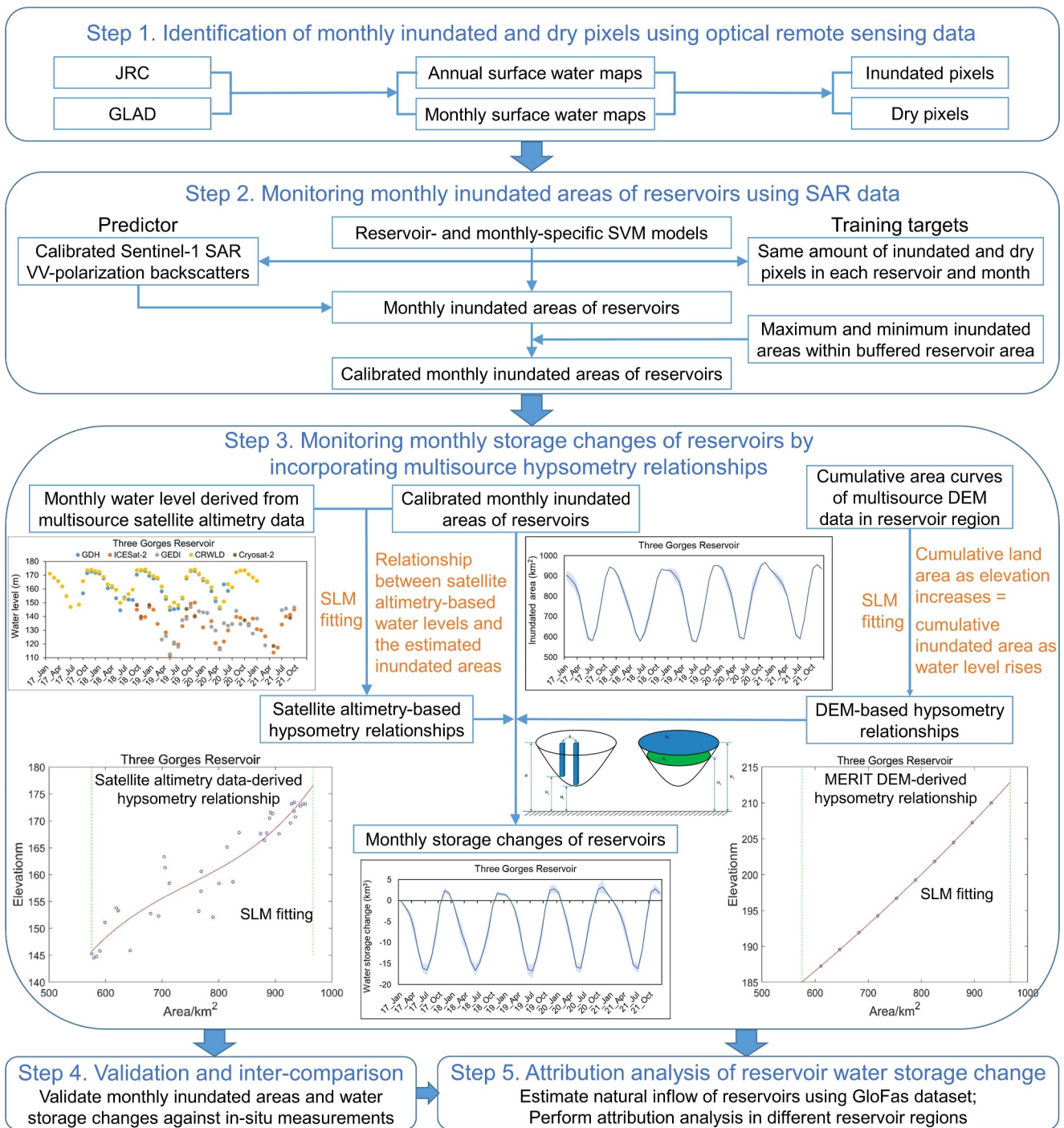


Figure 2. Conceptual diagram of this study (each step corresponds to a subsection). JRC, Joint Research Center (JRC)'s global surface water dynamics data set; GLAD, Global Land Analysis and Discovery team's global surface water dynamics data set; SVM, Support Vector Machine classification model; SLM, Shape Language Modeling fitting algorithm.

2.4. Satellite Altimetry and DEM Data Preprocessing

Obtaining accurate reservoir hypsometry relationship is pivotal for estimating water storage changes based on monthly inundated areas. Satellite altimetry data emerge as a primary choice for this purpose. During our study period from 2017 to 2021, active LiDAR missions in operation included ICESat-2 (Ice, Cloud, and land Elevation Satellite-2) and GEDI (Global Ecosystem Dynamics Investigation), while radar altimetry data were

predominantly sourced from missions such as CryoSat-2, Jason-2, Jason-3, SARAL, Sentinel-3A, and 3B. Among these missions, CryoSat-2, ICESat-2, and GEDI stood out due to their distinctive advantages. CryoSat-2, launched by ESA in April 2010, boasts a minimal orbital gap, with an equatorial gap of only 7.5 km, allowing for the observation of a greater number of reservoirs. However, this advantage is balanced by a longer revisit period of 369 days (L. Jiang et al., 2017; X. Li et al., 2019). ICESat-2, a NASA endeavor launched in September 2018, is equipped with a single-photon LiDAR system known as “ATLAS,” capable of emitting six laser beams with a narrow footprint diameter of only 17 m. This configuration facilitates high-accuracy surface water level retrieval over numerous relatively small water bodies (Cooley et al., 2021; Markus et al., 2017). GEDI, launched in December 2018 to the International Space Station, was primarily designed for observing forest canopy height but can also provide high-quality surface water level measurements (Fayad et al., 2020).

In our analysis, we selected specific data sets to harness the potential of these missions, including the CryoSat-2 Consolidated Level 2 Geophysical Data Record (GDR) (ESA, 2019), ICESat-2 L3A Along Track Inland Surface Water Data (ATL 13) V005 product (Jasinski et al., 2021), and the “elev_lowestmode” band from GEDI L2A Raster Canopy Top Height Version 2, which are available on the GEE (see Figures S3a and S3b in Supporting Information S1 for some examples of images). Our approach involved determining the monthly minimum inundated extent within each reservoir, as detailed in Section 3.1. We then extracted all CryoSat-2, ICESat-2, and GEDI measurements corresponding to these inundated pixels. For each reservoir, we applied the concentrated Probability Density Function (PDF) methodology (Z. Liu et al., 2019) to remove outliers and compute a robust estimate of the monthly mean water level. Subsequently, ICESat-2 and GEDI measurements underwent analogous processing. Figures S3c–S3f in Supporting Information S1 exhibit histograms of monthly ICESat-2 and CryoSat-2 altimetry data acquired in the Three Gorges Reservoir before and after performing the data filtering using the PDF method.

While other radar altimetry missions, including Jason-2 and 3, SARAL, Sentinel-3A, and 3B, feature larger orbital gaps and consequently cover fewer inland water bodies, they still contribute valuable altimetry data for certain reservoirs that CryoSat-2, ICESat-2, and GEDI may not have accessed. To ensure the reliability of water level data retrieved from these missions, we employed data products compiled by external research institutes or organizations. These data sets included the Global Reservoirs and Lakes Monitor (G-REALM) (Birkett et al., 2011, 2019), the Database for Hydrological Time Series of Inland Waters (DAHITI) (Schwatke et al., 2015), Le laboratoire d'études en géophysique et océanographie spatiales (LEGOS) Hydroweb (Crétau et al., 2011), and the China Reservoir Water Level Data set, abbreviated as CRWLD (Shen et al., 2022). Utilizing each of these data sets, we calculated monthly reservoir water levels as the medians of all high-quality altimetry records within each respective month.

In cases where satellite altimetry data lacked sufficient coverage for many reservoirs, the derivation of information on reservoir hypsometry relationships relied on alternative data sources, notably DEMs. However, since DEMs do not extend beneath the water surface, hypsometry relationships beneath the reservoir water level at the time of DEM retrieval are unknown. For some reservoirs, the lowest water level during the study period may be far below the reservoir water level at the time of DEM retrieval. To alleviate this limitation, we incorporated two distinct DEM data sources acquired at different times to facilitate generation of reservoir hypsometry relationships. The first one is the Multi-Error-Removed Improved-Terrain (MERIT) DEM, an enhanced version of the Shuttle Radar Topography Mission (SRTM) DEM referencing the year 2000 (Yamazaki et al., 2017). The second one is the Copernicus DEMs, which is developed by ESA based on observations from twin radar satellites, Tandem-X and TerraSAR-X, during the period spanning 2011–2015 (ESA, 2021).

2.5. Other Data Sources

To validate the estimated monthly inundated areas and water storage changes of large reservoirs in China, we collected daily records of reservoir water level and storage spanning from 2017 to 2021. These data were sourced from authoritative entities such as the Ministry of Water Resources-National Hydrological Information Center (MWR-NHIC, 2023) (http://xxfb.mwr.cn/sq_dxsk.html), the Yellow River Conservancy Commission (YRCC, 2023) (<http://61.163.88.227:8006/hwsq.aspx?>), and various provincial hydrological information websites (<http://yzt.hnswkcyj.com:9090/#/>, <http://www.schwr.com/article/45>, <http://113.57.190.228:8001/web/Report/BigMSKReport>). For our validation data set, we compiled water level data for 80 reservoirs where

monthly inundated areas could be estimated using our method. The locations of these validation reservoirs are depicted in Figure S4 in Supporting Information S1.

For comparison, we evaluated the quality of two global-scale data sets on monthly inundated areas of reservoirs: the Global Lake Evaporation Volume data set (GLEV) (G. Zhao et al., 2022) and the Global Reservoir Surface Area Data set (GRSAD) (G. Zhao & Gao, 2018). GLEV integrates annual maximum and minimum areas of water bodies with multi-year averaged intra-annual variations in inundated areas. In contrast, GRSAD establishes a threshold water occurrence based on available observations and fills missing data subsequently. Both data sets utilize Landsat data exclusively and cover the period from 1985 to 2018.

Additionally, we assessed the Reservoir data set in China (Res-CN), a multi-sensor approach-based data set encompassing monthly inundated areas and water storage changes for most reservoirs in China (Shen et al., 2023). Res-CN refines the GRSAD algorithm (Donchyts et al., 2022) by incorporating improvements and include data from both Landsat and Sentinel-2 images from 2017 to 2021. Water storage changes in Res-CN are estimated using satellite altimeter data from Sentinel-3A, Sentinel-3B, Jason-3, ICESat-2, CryoSat-2, and SARAL/AltiKa, as well as DEM data (Shen et al., 2023).

To conduct attribution analysis on the estimated reservoir water storage changes, we utilized the Global Flood Awareness System (GloFAS) version 4.0 data set provided by the European Center for Medium-Range Weather Forecasts (Grimaldi et al., 2022a) to estimate monthly natural discharge. GloFAS version 4.0 integrates 0.05° resolution inputs with the HTESSEL land surface model and the LISFLOOD hydrological and channel routing model (Alfieri et al., 2020; Harrigan et al., 2020). The utilization of different data sources in this study is summarized in Figure S5 in Supporting Information S1.

3. Methods

The developed methodology can be separated into five steps (Figure 2). For the first two steps, we combined optical remote sensing data with SAR data to retrieve monthly inundated areas in 721 out of 785 large reservoirs in China. For the third step, we utilized multisource hypsometry relationships to transform monthly inundated areas into water storage change estimates in 662 large reservoirs. For the last two steps, we performed data validation, inter-comparison as well as attribution analysis of reservoir water storage changes.

3.1. Identification of Monthly Inundated and Dry Pixels Using Optical Remote Sensing Data

We categorized all pixels within the potential extent of each reservoir as “reservoir pixels.” For a given reservoir pixel in a specific month, it was classified as either inundated or dry based on the conditions outlined in Figure 3, utilizing either the JRC or GLAD data sets. To establish these conditions, including determining the thresholds, we analyzed JRC and GLAD’s annual or monthly surface water maps (Figure S1 in Supporting Information S1). For instance, we observed that due to the limitations of optical remote sensing in detecting frozen water bodies, particularly those covered by snow, certain reservoirs (e.g., Xiangyangshan Reservoir in northeast China) showed pixels labeled with either no information or a water percent (indicating inundation probability) of less than 25% (mostly 0%) during winter according to GLAD’s monthly maps (Figure S6a in Supporting Information S1). This designation of all pixels as dry does not align with reality. Hence, considering the annual mean inundation frequency values in GLAD’s annual maps becomes crucial. Among these pixels, only those with an annual mean inundation frequency below 5% could be reliably identified as dry pixels. These few pixels were typically located around the boundary of the reservoir (Figure S6b in Supporting Information S1). In China, the frozen period of reservoirs, and even lakes, rarely lasts for half a year (Ruan et al., 2020; Q. Yang et al., 2019). Assuming there is a pixel in a reservoir that is frozen for half the year, its inundation probability is assigned a value of 0 throughout the frozen period. Then, if the reported annual water percent is 5%, the average observed inundation probability during non-frozen seasons should be approximately 10%. Even if the cloud frequency during the non-frozen season is twice that during the frozen season, which is uncommon in China (Xiao et al., 2018), the average observed inundation probability during non-frozen seasons should still be 20%. Accordingly, the likelihood that the real inundation probability in a frozen month is higher than 50% is expected to be very low.

However, relying solely on the annual water percentage is also unreliable, as some pixels may have a very low annual water percentage according to GLAD, but during specific months of that year, the predicted inundation probability can be considerably high (Figures S6c and S6d in Supporting Information S1). Therefore, in addition

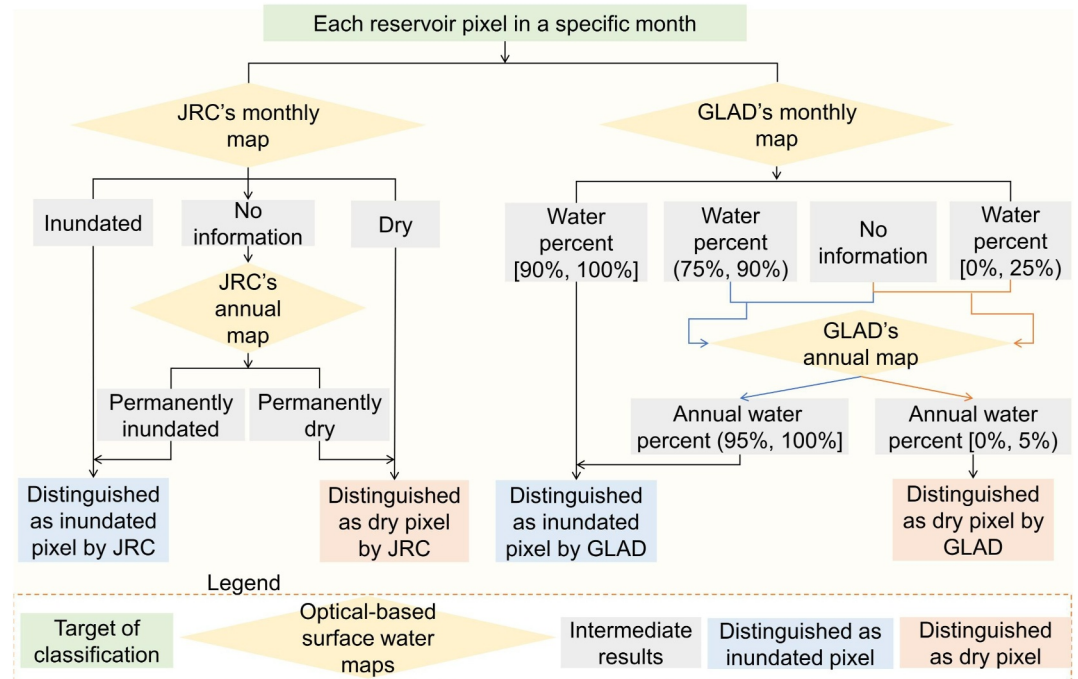


Figure 3. Identification of monthly inundated or dry reservoir pixels by using the Joint Research Center (JRC) and Global Land Analysis and Discovery (GLAD) data sets, respectively.

to the annual water percent, we have also included the monthly water percentage data reported in the GLAD data set for consideration. For a pixel that is not covered by clouds in a specific month, only if the reported monthly inundation probability is lower than 25% and at the same time the mean inundation frequency for that year is below 5% can it be classified as a high-confidence dry pixel. To sum up, this study uses both monthly inundation probability maps and annual mean inundation frequency maps to ensure a higher accuracy and reliability of the reference samples.

As illustrated in Figure 3, the identification based on GLAD is independent from that based on JRC, implying that certain pixels may be classified as inundated pixels by GLAD but as dry by JRC, and vice versa.

3.2. Monitoring Monthly Inundated Areas of Reservoirs Using SAR Data

The discrepancies in SAR backscatters between water and land can vary significantly among different reservoirs and seasons (Z. Jiang et al., 2021). To address this issue, we gathered information on inundated or dry reservoir pixels identified by the GLAD or JRC data sets for each reservoir and specific month. We then collected VV-polarized backscatters corresponding to these identified pixels. While optical remote sensing-based surface water identifications are generally more accurate, SAR backscatters are available across a broader range of locations and times. Consequently, we employed the optical remote sensing-based inundated and dry status as the training targets and VV backscatters as predictors. Given the 785 large reservoirs, 12 months, and two optical remote sensing-based training targets (GLAD-based identification results and JRC-based identification results), we compiled 18,840 ($785 \times 12 \times 2$) sets of training samples.

To ensure unbiased predictions (refer to Text S2 in Supporting Information S1 for detailed explanations), we maintained an equal number of inundated and dry pixels in each set of training samples. Specifically, for a given reservoir and month, if the count of inundated pixels identified by GLAD or JRC (referred to as No.inu) was lower than the count of dry pixels (No.dry), we randomly selected No.inu dry pixels from all dry pixels and combined them with all the inundated pixels to form the training sample set.

In instances where the minimum count between monthly No.inu and No.dry within a reservoir dropped below 50, we refrained from predicting the inundated or dry status for the reservoir's pixels during the corresponding month each year. Otherwise, we trained ten-fold support vector machine (SVM) models to predict the inundation

probability for each reservoir pixel, computed as the mean value of the 10 models' simulated results. Here, SVM serves as a supervised classification model, adept at identifying the best thresholds or a hyper-plane to separate two classes by maximizing the functional margin between the decision plane and the neighboring training data points (C.-C. Chang & Lin, 2011). SVM has been widely used in SAR-based surface inundation mapping (Aristizabal et al., 2020; Mountrakis et al., 2011).

The term “ten-fold” means that we partitioned the training data into 10 subsets, employing nine for training while reserving one-tenth for testing each time, and repeated this procedure 10 times to derive 10 distinct models. Ten-fold cross-validation stands as a dependable method for assessing machine learning model accuracy (Wong & Yeh, 2020). However, if the sample size for a class falls below 50, during ten-fold cross-validation, the average number of data points available for testing the omission or commission error of each model will be less than five, resulting in high uncertainty in the model's accuracy assessment. By setting this threshold to 50, we could generate 9,379 sets of ten-fold SVM models when using GLAD-based identification results as training targets, as well as 9,378 sets of ten-fold SVM models when using JRC-based identifications as training targets. Each set corresponds to a specific month and a reservoir. The total number accounts for 99.6% of the potential number, which is 18,840. Hence, setting the threshold at this level minimizes the number of reservoirs whose monthly inundated areas remain irretrievable compared to higher values.

After calculating the producer's accuracy (PA) and user's accuracy (UA) for each set of models based on the mean omission and commission errors of 10 individual models, SVM model sets were deemed of high quality if they met the following criteria: (a) $PA + UA \geq 180\%$ and (b) $|PA - UA| \leq 10\%$ (Bastarrika et al., 2011; Y. Wang et al., 2023). Conversely, lower quality model sets were discarded.

For each reservoir, in months with available inundation probability predictions, we calculated the inundated area by summing the inundation probabilities of reservoir pixels. We applied the “ 3σ principle” to detect and remove outliers in the resulting time series of inundated areas. Subsequently, we employed a Gaussian filter with a 5-month window size to smooth the time series. These steps were tailored for reservoirs where the simulation accuracy of inundation probability in certain months was limited. For a small subset of reservoirs with at least three consecutive months lacking valid predictions, the Gaussian smoother applied in this study could not produce a complete time series of monthly inundated areas.

To sum up, by separating SVM model training and simulations by month, screening for high-quality SVM models, and performing temporal filtering, we can alleviate the issue of low-quality inundation area simulations in some specific months (e.g., frozen months) caused by inaccurate optical-based reference samples.

The next step involved calibrating the maximum and minimum inundated areas of each reservoir. We introduced a 300 m buffer around each reservoir's extent (refer to Text S3 in Supporting Information S1 for detailed explanations) and determined the annual permanent and seasonal surface water areas within the entire extent using optical images (from the GLAD and JRC data sets). After calculating the minimum and maximum inundated areas for each reservoir, we used this information to linearly adjust the fluctuations in monthly reservoir inundated areas. Notably, we did not apply the buffer before this step (i.e., in the simulation of pixel-scale inundated probability using SAR backscatters), as the presence of wetlands and paddy fields within the additional buffer areas could disrupt the seasonal variation of reservoir inundated area estimates retrieved from SAR backscatters. However, this calibration is also essential because the shapefiles of some reservoirs reported in the CRD are likely too small to cover all the inundated pixels in these reservoirs when the water level is high. For example, the actual maximum inundated area of the Nuozhadu Reservoir in SW China is approximately 320 km² (Do et al., 2020; Y. Wang et al., 2023). However, the total area of the shapefile for this reservoir in the CRD is only 300 km².

Subsequently, we computed the R^2 values between each reservoir's monthly inundated area estimates over the period 2017–2021 when the GLAD data set was used as the training target and when the JRC data set was employed as the reference. If the R^2 reached 0.5, we calculated the mean of these two estimates (abbreviated as “SAR + JRC” and “SAR + GLAD”) as the final estimate. Otherwise, we selected the better estimate by comparing the numbers of valid monthly SVM models when using GLAD and JRC data as training targets, along with the mean overall accuracy of all 12 models if the numbers of valid models were equal. Uncertainties in the monthly inundated areas were computed following the method outlined in Text S4 in Supporting Information S1.

3.3. Monitoring Monthly Storage Changes of Reservoirs by Incorporating Multisource Hypsometry Relationships

Initially, we conducted regression analyses using monthly water levels derived from diverse satellite altimetry data sources, that is, G-REALM, DAHITI, Hydroweb (collectively abbreviated as GDH), ICESat-2, CryoSat-2, GEDI, and CRWLD, against estimated monthly inundated areas. Utilizing the Shape Language Modeling (SLM) algorithm (D'Errico, 2023), we fitted the hypsometry relationship, incorporating values beneath the lowest satellite-observed water level and above the highest satellite-observed water level, subject to specific conditions. These conditions comprised: (a) the variation range of inundated areas in months with altimetry data exceeding half of the total variation range of the inundated area during 2017–2021; (b) the presence of a significant correlation ($p < 0.05$, sample size ≥ 5) between available monthly water level data and corresponding inundated area estimates. We opted for the SLM fitting algorithm due to its utilization of least squares splines, facilitating the imposition of monotonic constraints on the fitted hypsometry relationship (D'Errico, 2023). SLM fitting encompassed both a monotonous cubic function (without knots) and a model featuring a knot in the middle, with preference given to the model exhibiting the higher R^2 value. To ensure the reliability of hypsometry relationships, we retained only the SLM fittings with an R^2 exceeding 0.5.

Subsequently, we employed Copernicus DEM data to derive reservoir hypsometry relationships. This process entailed extracting DEM values within the reservoir's extent to estimate the reservoir water level at the time of DEM retrieval, identified as the mode of these elevation values (referred to as the reference water level). If the fraction of pixels with elevations below the reference water level was less than 10%, indicating satisfactory DEM data quality (confidence $\geq 90\%$), we calculated the reservoir's reference inundated area as the total area of pixels with elevations equal to or below the reference water level. We then utilized the SLM algorithm to fit the cumulative area curve of elevation values above the reference water level. The fitted curve represents the cumulative land area as elevation increases, and corresponds to the cumulative inundated area as the water level rises. If the difference between the reference inundated area and the minimum monthly inundated area during 2017–2021 was smaller than that between the maximum monthly inundated area and the reference area, the fitting model was anticipated to effectively predict variations in water level when the inundated area fluctuated between the minimum monthly inundated area and the reference inundated area. Thus, the hypsometry relationship could be established.

We also incorporated the SRTM DEM-based MERIT DEM to estimate reservoir hypsometry relationships. This process entailed segregating elevation data for inundated and dry pixels using the SRTM Water Body Data Shapefiles and Raster Files (SRTMSWBD v003) (NASA, 2013), and then removing elevation values that are lower than or equal to the elevation of the water surface. An example of MERIT-DEM data with inundated pixels removed around the Three Gorges Reservoir is shown in Figure S7 in Supporting Information S1. Following this, we conducted quality checks and applied a similar algorithm as used with the Copernicus DEM to fit the reservoir hypsometry relationship based on the MERIT DEM.

Using hypsometry relationships derived from various sources, we converted monthly reservoir inundated areas into water level changes. The water storage change ($\Delta V_{r,m}$) in reservoir r from the previous month ($m - 1$) to the current month (m) was calculated using the formula: $\Delta V_{r,m} = (H_{r,m} - H_{r,m-1}) \times \frac{A_{r,m-1} + A_{r,m} + \sqrt{A_{r,m-1} \times A_{r,m}}}{3}$, where A represents the inundated area, and H represents the water level (Taube, 2000). Estimates where the range of the estimated water storage variation in a reservoir exceeded 110% of its total storage were considered unconvincing, and the corresponding hypsometry relationship estimates were discarded.

Validation against in-situ measurements of reservoir water storage changes (see Section 3.4 for methods) indicated that the satellite altimetry-based hypsometry relationships generally outperformed DEM-derived hypsometry relationships, with the MERIT DEM being more accurate than the Copernicus DEM (Section 4.2 provides the comparison results). To generate a robust estimate of reservoir water storage changes, we employed the following approach: if we had at least two hypsometry relationships derived from various satellite altimetry data, we adopted the median of the corresponding water storage change estimates. If a MERIT DEM-based hypsometry relationship was also unavailable, we incorporated the estimate derived using the Copernicus DEM. Uncertainties of monthly water storage changes were calculated following Text S4 in Supporting Information S1.

3.4. Validation and Inter-Comparison

To validate the estimated inundated areas, we calculated the Spearman Correlation Coefficient (CC) between the estimated inundated areas and the in-situ water levels at 80 large reservoirs. Among these reservoirs, 78 also had water storage data available. Thus, we assessed the accuracy of the estimated reservoir water storage changes by comparing them to the in-situ water storages at these 78 reservoirs. For this comparison, we used both the coefficient of determination (R^2) and the relative root mean square error (rRMSE), which is the ratio of RMSE to the mean reservoir water storage.

For inter-comparison, we also validated the inundated area estimates of Chinese large reservoirs in both the GLEV and GRSAD data sets, as well as the reservoir inundated area and water storage change estimates in the Res-CN data set.

3.5. Attribution Analysis of Reservoir Water Storage Changes

Reservoir water storage changes primarily stem from two key factors: natural inflow and anthropogenic influences such as outflow control, water withdrawal, and water diversion. Natural inflow is influenced by several factors, including precipitation, snow or ice melt, evapotranspiration, and seepage within the upstream watershed of the reservoir. Our method involved extracting the maximum discharge value reported by the GloFAS data set within each reservoir's extent to represent the natural inflow into the reservoir. Subsequently, we aggregated daily inflow data to compute monthly totals. The variation in reservoir total water storage in each region (refer to regional classification in Figure 1) that cannot be explained by natural inflow changes could be mainly attributed to anthropogenic impacts. Although currently, there are no data providing detailed water management and withdrawal information for various large reservoirs throughout China (Dong et al., 2022; Qi et al., 2021), we attempted to justify our inferences by referring to published literature documenting basic characteristics (e.g., impoundment time and major functions) of some typical large reservoirs in different regions. See Section 5.2 and Text S1 in Supporting Information S1.

4. Results

4.1. Quantity and Quality of Estimated Reservoir Monthly Inundated Areas and Water Storage Changes

Variations in the producer's accuracy (PA) and UA metrics across all SVM models for estimating monthly inundated areas in reservoirs (Figure 4) reveal that when employing SAR backscatters in combination with the GLAD data set, the medians of PA consistently ranged from 0.97 to 0.98. These values were notably higher during the summer months but exhibited a slight decrease in the winter season. Concurrently, the medians of UA consistently surpassed 0.99 throughout the entire year. Conversely, when using surface water identifications based on the JRC data set as the training target, the medians of both PA and UA for all large reservoirs were marginally lower. Median PA values ranged from 0.93 to 0.95, depending on the season, while median UA values ranged from 0.96 to 0.97. These results underscore the overall high accuracy achieved by SVM models, indicative of the reliability of inundated area estimation, particularly during non-frozen seasons.

Among the 785 large reservoirs in China, our method successfully obtained monthly inundated area estimates for 719 and 678 reservoirs when utilizing the GLAD and JRC data sets as references, respectively. In total, we estimated monthly inundated areas for 721 large reservoirs in this study, representing 95% of the combined storage capacity of all 785 reservoirs. Notably, 628 reservoirs exhibited an R^2 value exceeding 0.5 when comparing estimates derived from SAR + GLAD with those from SAR + JRC, indicating higher-quality inundated area estimates for these reservoirs, which collectively account for 82% of the total storage capacity of all large reservoirs.

Out of the 721 large reservoirs under monthly inundated area monitoring, hypsometry relationship information was successfully obtained for 662 reservoirs. The sources of hypsometry relationship data included the GDH data set, ICESat-2, CryoSat-2, GEDI, CRWLD, MERIT DEM, and Copernicus DEM, providing hypsometry relationship estimates for 26, 148, 68, 54, 94, 627, and 270 reservoirs, respectively. As illustrated in Figures 6c and 6d, satellite altimetry data-derived hypsometry relationships generally outperformed DEM-based hypsometry relationships. Among different DEM-based hypsometry relationships, estimates derived from the MERIT DEM

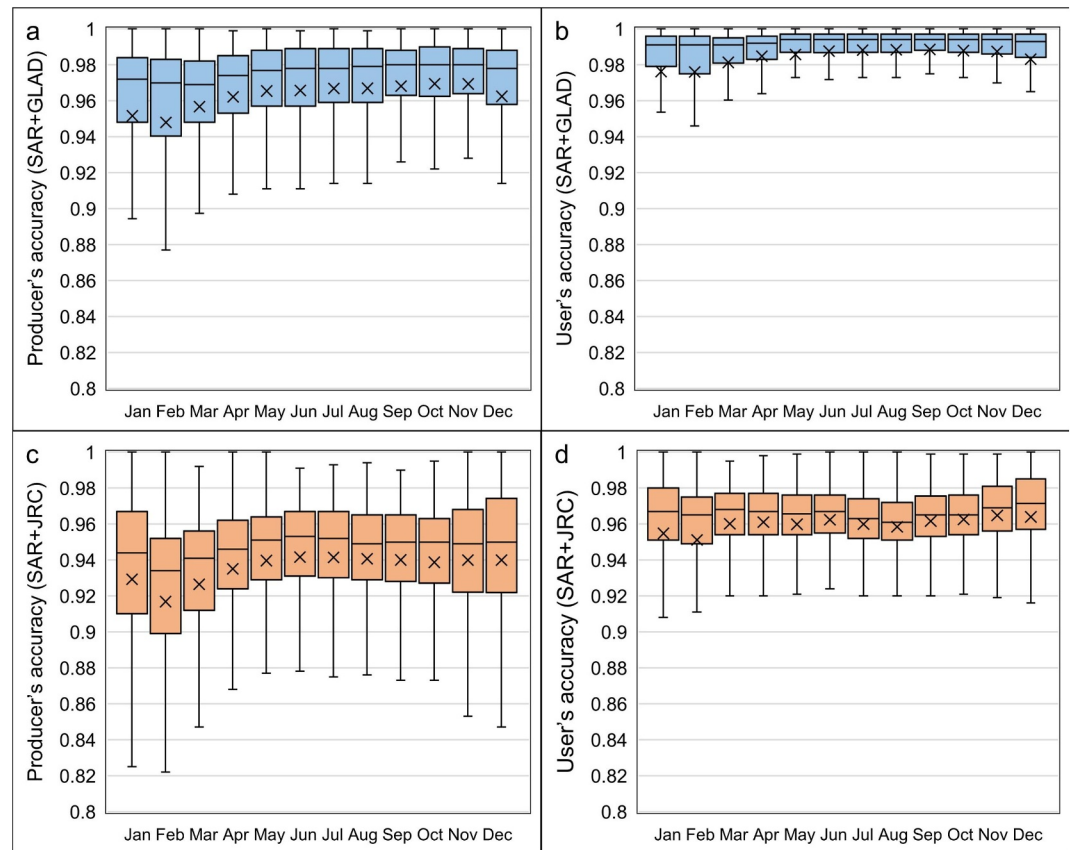


Figure 4. Producer's and User's Accuracy (PA and UA) of monthly support vector machine models for all 785 reservoirs when an equal amount of inundation and dry status identifications were included as training targets. These accuracy estimates were derived from the testing data during the 10-fold cross validation. Synthetic aperture radar (SAR) + Joint Research Center (JRC) and SAR + Global Land Analysis and Discovery (GLAD) denote scenarios in which surface water identifications based on the JRC and GLAD data sets were utilized, respectively.

generally exhibited higher reliability compared to those derived from Copernicus DEM data. Therefore, based on the origin of the hypsometry relationship data, we categorized the quality of reservoir hypsometry relationship estimates into seven levels (Table 1). Notably, Q1 represents the highest quality level, while Q1 through Q4 are designated as high quality. Reservoirs classified under Q5 through Q7 are associated with just one hypsometry relationship estimate, consequently considered to have lower-quality estimates.

As shown in Table 1, we successfully acquired high-quality hypsometry relationship estimates for 395 reservoirs, while 267 reservoirs were associated with lower-quality hypsometry relationship data. Remarkably, 360 reservoirs boasted high-quality estimates for both monthly inundated areas and reservoir hypsometry relationships (Figure 5). While the proportion of reservoirs benefiting from high-quality water storage change monitoring was relatively modest (46%), these reservoirs collectively represent a substantial 70% of the total storage capacity across all large reservoirs in China.

4.2. Validation of Monthly Inundated Areas and Water Storage Changes in Reservoirs

Among the 80 validation sites illustrated in Figure S4 in Supporting Information S1, the Spearman CC between the estimated monthly inundated areas and the measured water levels exceeded 0.7 for 72 reservoirs. As shown in Figure 6a, the Spearman CC for the monthly inundated areas estimated in this study reached 0.85 ± 0.13 (median: 0.89). Moreover, our approach consistently achieves high-accuracy monthly inundated area monitoring ($CC > 0.8$) across reservoirs of varying sizes (Figure 6b).

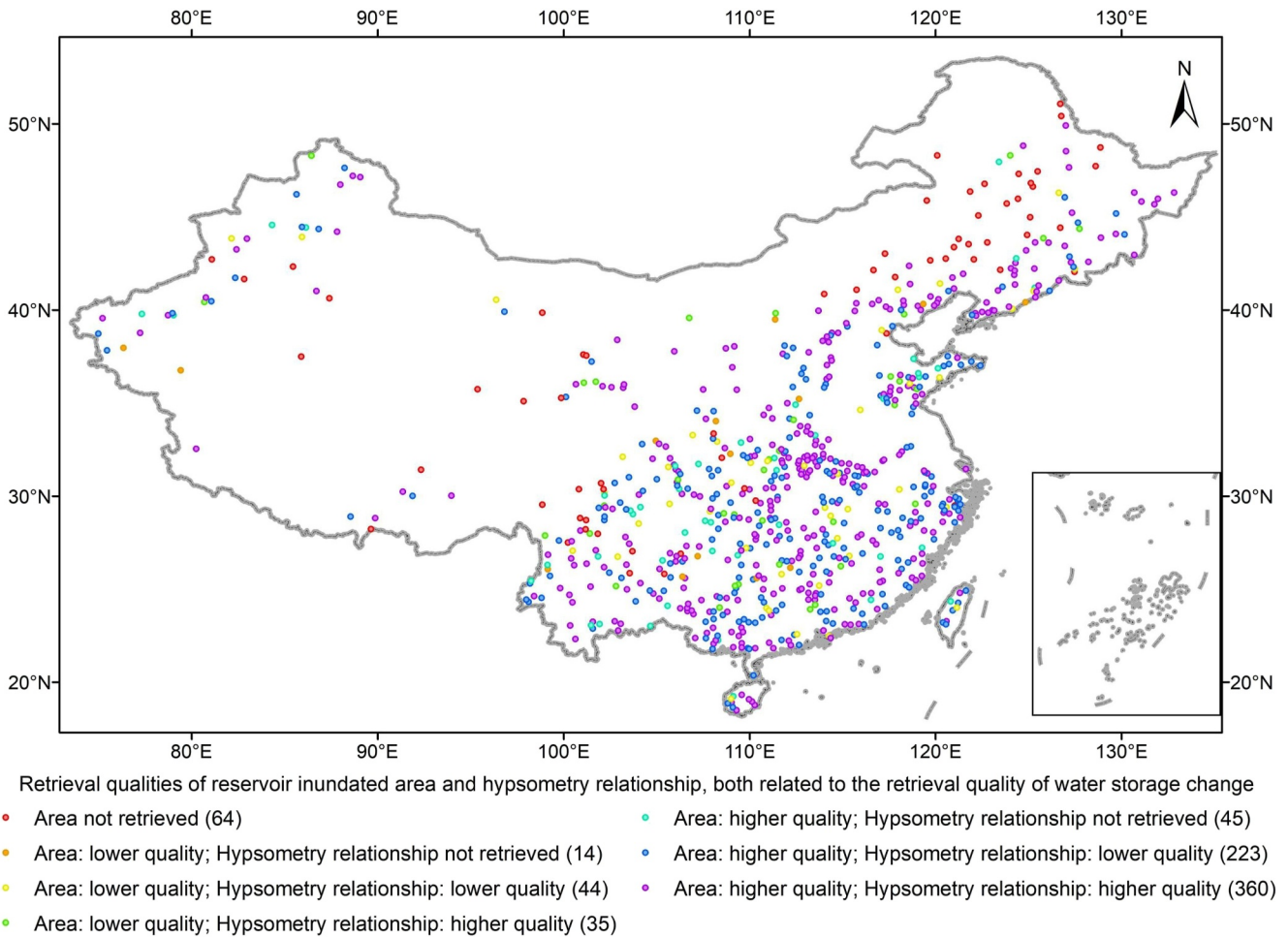


Figure 5. Quality assessment of monthly inundated areas and water storage changes across 785 large reservoirs in China. The numbers in the legend represent the count of reservoirs falling into each category.

Regarding the data comparison in Figures 6c and 6d, satellite altimetry data emerge as superior to DEM data in estimating reservoir hypsometry relationships. However, the availability of adequate altimetry records during the study period is limited. On the other hand, hypsometry relationships derived from the MERIT DEM generally exhibits higher reliability than estimates based on the Copernicus DEM. After combining hypsometry relationship

Table 1
Quality Category of Hypsometry Relationships for 662 Reservoirs

Quality category	Description	Number of reservoirs
Q1	Hypsometry relationships can be derived from at least two different satellite altimetry data sources	101
Q2	Hypsometry relationships were derived from one satellite altimetry data source and MERIT-DEM	112
Q3	Hypsometry relationships were derived from one satellite altimetry data source and Copernicus-DEM	6
Q4	Hypsometry relationships were derived from both MERIT-DEM and Copernicus-DEM	176
Q5	Hypsometry relationships were derived from only one satellite altimetry data source	16
Q6	Hypsometry relationships were derived only from MERIT-DEM	244
Q7	Hypsometry relationships were derived only from Copernicus DEM	7

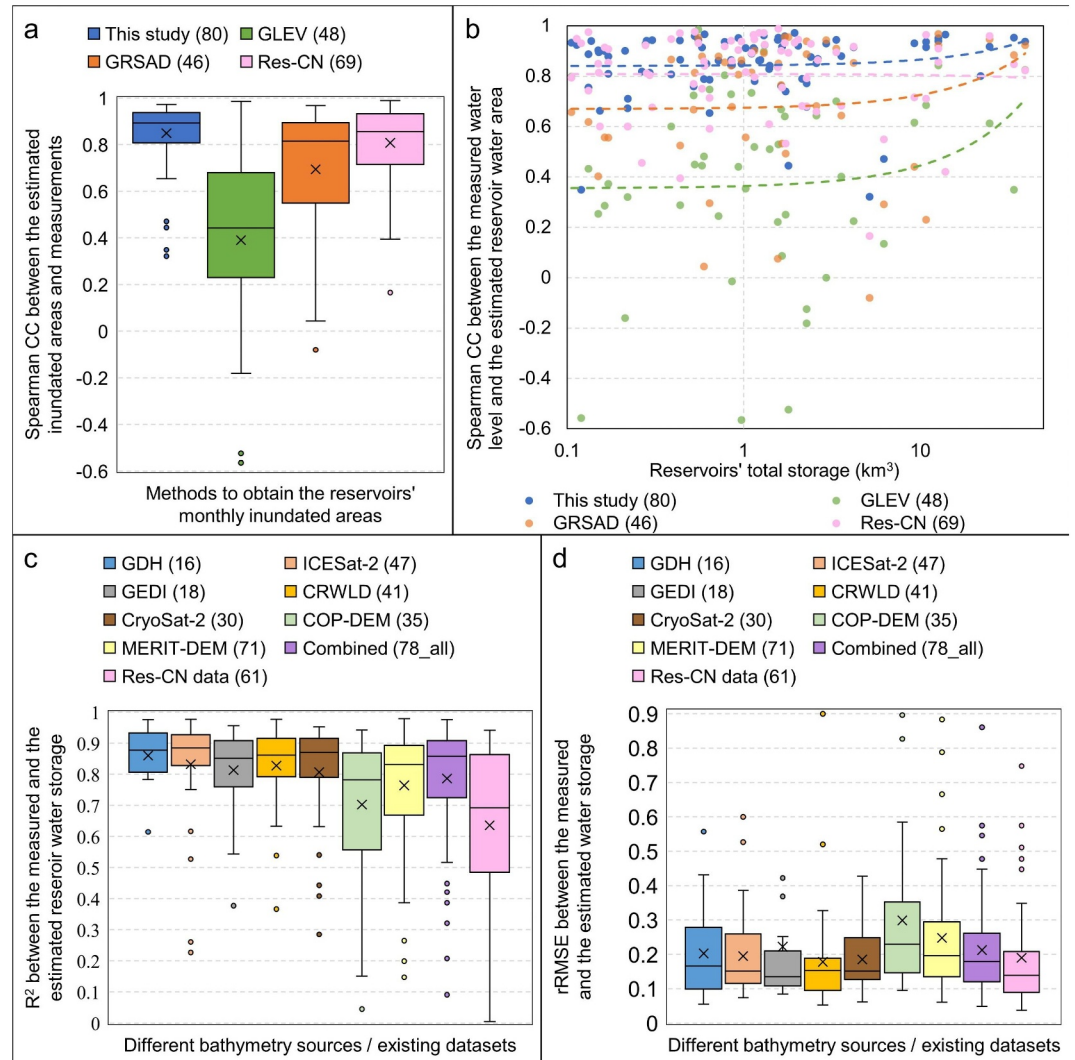


Figure 6. Validation results for monthly inundated area and water storage changes estimated in this study, alongside some previous studies, at 80 reservoirs in China. (a, b) Spearman correlation coefficient (CC) for estimated monthly inundated areas in relation to reservoir total storage capacity, including comparisons with the Global Lake Evaporation Volume data set (GLEV), Global Reservoir Surface Area Data set (GRSAD), and Reservoir data set in China (Res-CN) data sets. (c, d) Coefficient of determination (R^2) and relative root mean square errors (rRMSEs) for our monthly water storage change estimates using various hypsometry relationship data sources and the monthly water storage change estimates in the Res-CN data set. In figure legends, “Combined” denotes the final result in this study by integrating all sources of reservoir hypsometry relationships, with numbers in brackets indicating the validation set sizes.

data from different sources, our final estimates of monthly reservoir water storage changes achieve an R^2 of 0.79 ± 0.18 (median: 0.86) and a rRMSE of $21\% \pm 14\%$ (median: 18%).

4.3. Monthly Inundated Areas and Water Storage Changes of Large Reservoirs Across China

In Figures 7a and 7b and Figures S8a and S8b in Supporting Information S1, it is evident that the total inundated area of the 721 large reservoirs in China exhibited a significant decrease ($p < 0.01$) at a rate of $153 \pm 86 \text{ km}^2$ per year ($0.6 \pm 0.3\%$ of the total reservoir area) during 2017–2019. Subsequently, it rebounded by $290 \pm 197 \text{ km}^2$ per year ($1.1 \pm 0.7\%$ per year, $p < 0.01$). The overall change over the entire study period is statistically non-significant ($p = 0.06$). Conversely, the total water storage of large reservoirs reduced by $14 \pm 10 \text{ km}^3$ ($1.9 \pm 1.4\%$ of the total storage capacity) in 2017, followed by a significant rise of $3.5 \pm 2.6 \text{ km}^3$ per year ($1.5 \pm 0.4\%$ per year, $p < 0.01$). Consequently, the total water storage increased at a rate of $2.3 \pm 1.7 \text{ km}^3$ per year ($0.3 \pm 0.2\%$ per year, $p = 0.01$).

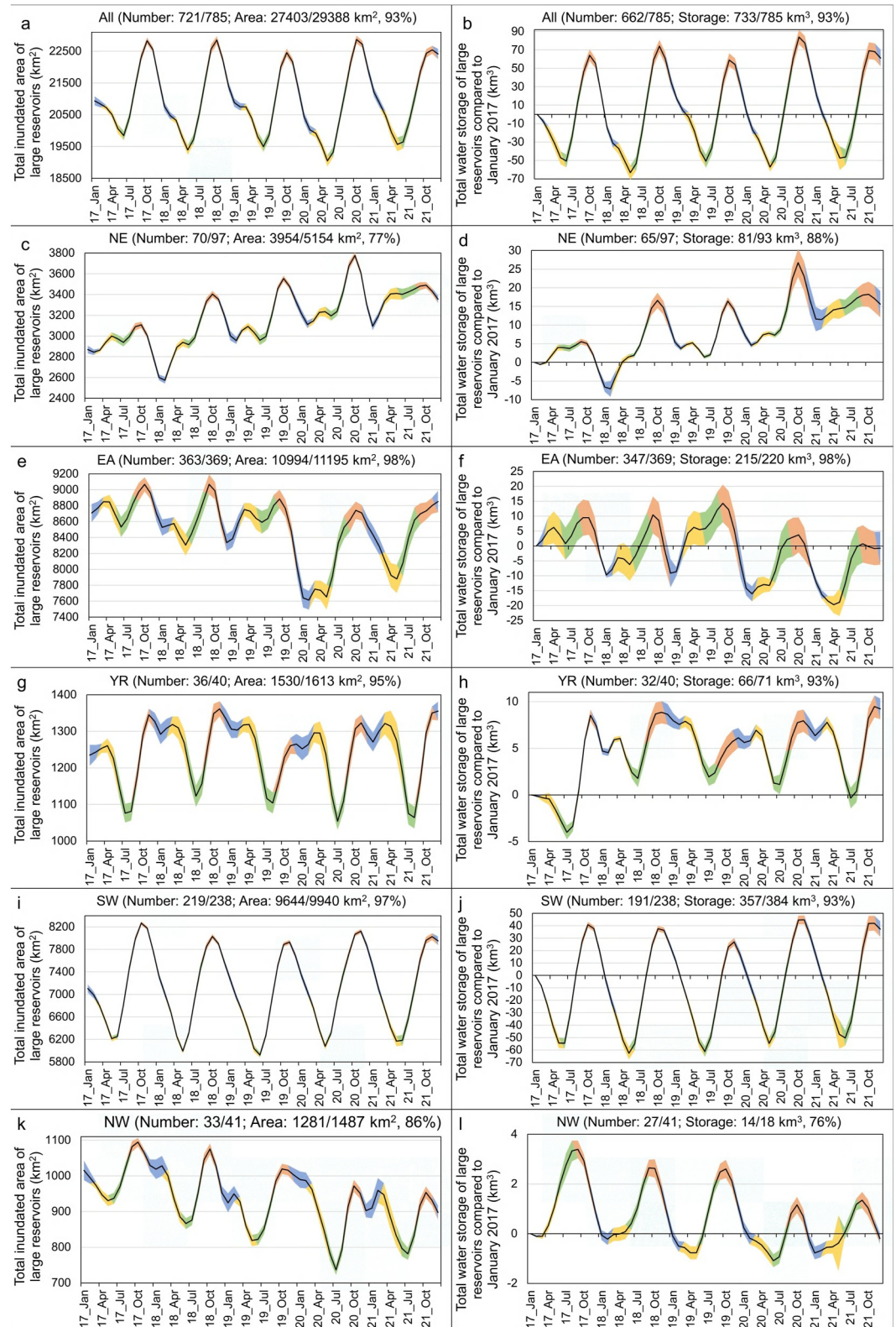


Figure 7.

during the entire study period. There exists a discrepancy between the overall trend of inundated area and the trend of water storage for all large reservoirs in China. However, for each individual reservoir, an expansion of the inundated area must be accompanied by an increase in water storage. Therefore, these observations indicate that shallower reservoirs in China were generally shrinking, while deeper ones were expanding. The increase in water storage of deeper reservoirs exceeded the water storage decline in shallower reservoirs, while the inundated area gains of deeper reservoirs were unable to offset the area shrinkage of shallower reservoirs. In each year, both the inundated area and water storage of large reservoirs increase from May/June to October and then decline during winter and spring.

In Northeast China (NE), large reservoirs witnessed an expansion in both inundated area and water storage, with rates of $113 \pm 20 \text{ km}^2$ per year ($2.9 \pm 0.5\%$ per year) and $3.2 \pm 0.6 \text{ km}^3$ per year ($4.0 \pm 0.8\%$ per year) over the entire study period. During 2018–2021, this expansion was particularly pronounced, reaching rates of $124 \pm 26 \text{ km}^2$ per year ($3.1 \pm 0.7\%$ per year) and $3.6 \pm 0.7 \text{ km}^3$ per year ($4.4 \pm 0.9\%$ per year). In each year, the total water storage peaked in October, although the peak's prominence was much weaker in 2017 and 2021. Conversely, the lowest reservoir water storage was often observed in February, except for 2019, when noticeable water storage loss occurred between April and June (Figures 7c and 7d and Figures S8c and S8d in Supporting Information S1).

In Eastern China (EA), the total inundated area exhibited a continuous reduction of $120 \pm 45 \text{ km}^2$ per year ($1.1 \pm 0.4\%$ per year) throughout the study period. Concurrently, total water storage decreased at a rate of $2.9 \pm 0.9 \text{ km}^3$ per year ($1.3 \pm 0.4\%$ per year), largely offsetting the reservoir expansion observed in NE. In EA, both the total inundated area and water storage reached their highest levels in October. However, during the first 3 years, a small peak was observed in March or April, which disappeared in 2020 and 2021 (Figures 7e and 7f and Figures S8e and S8f in Supporting Information S1).

In the YR, large reservoirs experienced increases in both inundated area and water storage at rates of $50 \pm 10 \text{ km}^2$ per year ($3.3 \pm 0.6\%$ per year) and $4.6 \pm 0.9 \text{ km}^3$ per year ($6.9 \pm 1.3\%$ per year), respectively, during 2017–2018. These trends remained stable thereafter ($p \geq 0.3$). Over the entire study period, changes in reservoir inundated area were statistically non-significant ($p = 0.7$), while total reservoir water storage increased at a rate of $0.9 \pm 0.4 \text{ km}^3$ per year ($1.3 \pm 0.5\%$ per year, $p < 0.01$). Intra-annually, reservoir inundated area and water storage exhibited two peaks, one in November and another in March–April, with the lowest values observed in July–August (Figures 7g and 7h and Figures S8g and S8h in Supporting Information S1).

In Southwest China (SW), the total water storage of large reservoirs showed slight increases at rates of $1.5 \pm 1.3 \text{ km}^3$ per year ($0.4 \pm 0.4\%$ per year, $p = 0.03$) during 2017–2021, while the inundated area remained relatively stable ($p = 0.39$). However, in 2019, both the inundated area in June–September and water storage in July–October were significantly lower than the multi-year averages. In this region, the seasonal variations of inundated area and water storage were consistent among different years, with peak values occurring in October–November and trough values in May–June (Figures 7i and 7j and Figures S8i and S8j in Supporting Information S1). Given that the storage capacity of local reservoirs accounts for 49% of the national total, the regional seasonal variation pattern significantly influences that of the entire country.

Northwest China (NW) experienced continuous reservoir shrinkage over the study period ($p < 0.01$), with declining rates of reservoir inundated area and water storage at $30 \pm 6 \text{ km}^2$ per year ($2.3 \pm 0.5\%$ per year) and $0.4 \pm 0.1 \text{ km}^3$ per year ($2.7 \pm 0.7\%$ per year), respectively. In each year, regional total water storage peaked in October, while the valleys occurred in different months, ranging from January–February in 2017, 2018, and 2021 to June in 2020. Similarly, the total reservoir inundated area was highest in October but was typically at its lowest from May–July (Figures 7k and 7l and Figures S8k and S8l in Supporting Information S1).

Additionally, monthly variations in inundated area and water storage for one typical large reservoir representing each region (i.e., the Shuifeng Reservoir in NE, the Xinfengjiang Reservoir in EA, the Liujiaxia Reservoir in YR,

Figure 7. Monthly calculated (a, c, e, g, i, k) inundated area and (b, d, f, h, j, l) water storage changes of large reservoirs (a, b) in China and (c–l) in different regions of China. Regions are classified as in Figure 1. The titles of each subfigure include the number and total inundated area or storage capacity of all regional large reservoirs, with the numbers before the slashes indicating the number and total inundated area or storage capacity of the reservoirs for which inundated area or water storage changes were calculated in this study. The shaded areas represent result uncertainties, with yellow, green, red, and blue indicating spring (March–May), summer (June–August), autumn (September–November), and winter (December–February), respectively.

the Wudongde Reservoir in SW, and the Xiaohaizi Reservoir in NW) are displayed in Figure S9 in Supporting Information S1.

5. Discussion

5.1. Comparison With Existing Data Sets

The Spearman CC for the monthly inundated areas estimated in this study (0.85 ± 0.13 , median: 0.89) is higher than those of GLEV (0.39 ± 0.37 , median: 0.44) and GRSAD data sets (0.69 ± 0.27 , median: 0.81), and the differences are both very significant ($p < 0.01$, Figure 6a). Our inundated area estimates are also significantly ($p = 0.04$) superior to those in the Res-CN data set, whose Spearman CC is 0.81 ± 0.16 (median: 0.85). While GRSAD demonstrates relatively reliable estimates for very large reservoirs, its accuracy diminishes significantly as reservoir size decreases (Figure 6b). Conversely, although Res-CN predicts inundated area variations in reservoirs smaller than 1 km^3 with similar accuracy as this study, its accuracy over very large reservoirs are lower compared to our data set (Figure 6b).

As shown in Figures 6c and 6d, the R^2 values of reservoir monthly water storage changes predicted by Res-CN (0.64 ± 0.26 , median: 0.68) are lower than this study (0.79 ± 0.18 , median: 0.86), and the difference is very significant ($p < 0.01$). The rRMSE of Res-CN water storage change data (0.19 ± 0.15 , median: 0.14) is somewhat lower than that of our estimates (0.21 ± 0.14 , median: 0.18), yet the difference is not significant ($p = 0.27$). These results suggest that our estimates of reservoir water storage changes are generally improved compared to Res-CN, although the incorporation of more satellite altimetry data (e.g., Sentinel-3 and SARAL/AltiKa) and the manual selection of altimetry records that are the most approximate to in-situ measurements (Shen et al., 2023) have probably ensured a better estimate of reservoir hypsometry relationships in Res-CN. In addition, while Res-CN involves some medium/small-sized reservoirs in China, 262 out of 785 large reservoirs in China are missing in this data set, which are mainly distributed in northeast and western China (see Figure S10 in Supporting Information S1). Water storage changes in only 462 large reservoirs have been provided by Res-CN, compared to 662 large reservoirs in this study.

In general, the comparison with existing data sets suggests that our monthly inundated area retrieval achieved an unprecedented accuracy. In terms of hypsometry relationship estimation, more high-quality satellite altimetry data sets (e.g., Sentinel-3) should be included because DEM-based hypsometry relationships often contain higher uncertainty.

5.2. Potential Drivers of Reservoir Water Storage Changes Across China

This study has unveiled the monthly water storage changes in large reservoirs across China for the period 2017–2021. As Figure 7 illustrates, both the inter-annual and intra-annual fluctuations of reservoir water storage exhibit significant regional disparities within China. In this section, we delve into investigating the potential driving factors behind the observed variations in reservoir water storage across different regions.

First, as indicated by the anomalies in natural inflow, illustrated in Figure S11 in Supporting Information S1, the significant expansion of reservoirs in NE during 2017–2020 can be largely attributed to the lowest natural inflow in 2017 and the subsequent surge in inflow during the summer of 2020. In NW, the inter-annual variation in natural inflow correlated well with changes in reservoir water storage. Therefore, the decrease in natural inflow in NW was a major factor contributing to the decline in water storage in local reservoirs (Table 2). Notably, in NE the fluctuations in reservoir water storage between July and October are significantly influenced by the cumulative natural inflow during these months (Figure 8a). In NW it is the inflow from January to August that predominantly shapes regional reservoir water gains during this period (Figure 8e). It is important to acknowledge that NW, characterized as the driest region in China, primarily relies on its reservoirs to supply irrigation water (S. Li et al., 2024; Yu et al., 2017). Additionally, inflow rates into NE reservoirs are relatively modest, averaging approximately $3 \text{ km}^3/\text{year}$ per reservoir, as opposed to the higher inflow rates estimated in southern regions ranging from 6 to $25 \text{ km}^3/\text{year}$ per reservoir. Consequently, reservoirs in NW and NE were mainly built for water storage and supply or hydropower production rather than flood control (see Text S1 in Supporting Information S1), resulting in lower anthropogenic water releases to downstream rivers before rainy seasons (Dong et al., 2022). The intra-annual fluctuations in reservoir water storage in NE and NW are also significantly influenced by natural inflow. In NE, the reduced seasonal variability in water storage during 2017 and 2021 can be

Table 2
Trends in Reservoir Water Storage Anomalies and Natural Inflow Anomalies Across Various Regions of China From 2017 to 2021

Region	Trend in water storage anomalies	Trend in natural inflow anomalies
NE	$3.2 \pm 0.6 \text{ km}^3/\text{year}$ ($4.0 \pm 0.8\%/ \text{year}$)**	$24.4 \pm 16.2 \text{ km}^3/\text{year}$ ($11.6 \pm 7.7\%/ \text{year}$)**
EA	$-2.9 \pm 0.9 \text{ km}^3/\text{year}$ ($-1.3 \pm 0.4\%/ \text{year}$)**	$-5.0 \pm 91.2 \text{ km}^3/\text{year}$ ($-0.3 \pm 4.7\%/ \text{year}$)
YR	$0.9 \pm 0.4 \text{ km}^3/\text{year}$ ($1.3 \pm 0.5\%/ \text{year}$)**	$46.2 \pm 18.7 \text{ km}^3/\text{year}$ ($11.1 \pm 4.5\%/ \text{year}$)**
SW	$1.5 \pm 1.3 \text{ km}^3/\text{year}$ ($0.4 \pm 0.4\%/ \text{year}$)*	$123.2 \pm 132.0 \text{ km}^3/\text{year}$ ($2.6 \pm 2.8\%/ \text{year}$)
NW	$-0.4 \pm 0.1 \text{ km}^3/\text{year}$ ($-2.7 \pm 0.7\%/ \text{year}$)**	$-7.8 \pm 4.8 \text{ km}^3/\text{year}$ ($-6.3 \pm 3.9\%/ \text{year}$)**
China	$2.3 \pm 1.7 \text{ km}^3/\text{year}$ ($0.3 \pm 0.2\%/ \text{year}$)*	$181.0 \pm 204.4 \text{ km}^3/\text{year}$ ($2.5 \pm 2.8\%/ \text{year}$)

Note. Trends with one and two asterisks are statistically significant at the 95% and 99% confidence level, respectively.

attributed to lower inflow in summers and higher inflow in spring or fall. Notably, the spring drought in 2019 contributed to the lowest local reservoir water storage observed in June (Figure 9b). Similarly, in NW, the continuous reservoir water storage loss from January to June in 2020 was primarily due to low natural inflow (Figures 9i and 9j).

The natural inflow in EA did not experience significant changes (Table 2), suggesting that anthropogenic factors (e.g., more water abstraction and impoundment of upstream reservoirs (X. Yang & Lu, 2014; X. Yang et al., 2020)) played a dominant role in the significant decline in reservoir water storage in EA during 2017–2021. In the YR, although both natural inflow and reservoir water storage exhibited significant trends over the entire study period, water storage primarily increased during 2017–2018 when natural inflow was relatively low. The impoundment completion of the Longyangxia Reservoir over this period (S. Zhao et al., 2022) is presumed to be the primary cause. In both EA and the YR, the reservoir water storage changes from June to September and from March to June exhibit negative correlations with the corresponding variations in natural inflow ($p < 0.05$, Figures 8b and 8c). These correlations suggest that the outflow from reservoirs during or before the rainy season is properly adjusted based on the inflow data to mitigate downstream flooding risks and ensure the structural integrity of the dams (refer to Text S1 in Supporting Information S1) (Dong et al., 2022; P. Liu et al., 2015; X. Wang et al., 2011; L. Yang et al., 2021). Intriguingly, following the rainy season, due to restricted outflow, a significant positive impact of natural inflow re-emerges in EA (Figure 8b). Additionally, we observed that during 2017–2019, the spring natural inflow in EA largely contributed to the height of the reservoir water storage peak in March–May (Figures 8b, 9c, and 9d). However, this peak disappeared after 2019, suggesting an intensified anthropogenic water release before the rainy season. Finally, the double peak pattern in the seasonal variation of YR reservoirs is likely due to human control measures for ice-jam prevention (J. Chang et al., 2016).

The significant increase in reservoir water storage in SW during 2017–2021 (Table 2) could be mainly attributed to the impoundment of large hydropower stations (Dai et al., 2023). In addition, the reservoir water storage changes during different seasons are not significantly correlated with the corresponding variations in natural inflow (Figure 8d). This phenomenon suggests that reservoirs in the southwest region are subject to rigorous management practices, potentially oriented toward power generation and flood control purposes (Dong et al., 2022; Fang & Deng, 2011; P. Liu et al., 2015; X. Wang et al., 2011). However, a summer drought in 2019 led to a significant decline in reservoir water storage in SW from July to October. This decline was offset by the high natural inflow in 2020. Obviously, in addition to anthropogenic factors, variations in meteorological conditions also play a significant role in the interannual variation in reservoir water storage in SW.

In conclusion, natural inflow significantly impacts both the inter-annual and intra-annual variations of reservoir water storage in NE and NW. However, anthropogenic factors such as outflow control and water withdrawal for multiple purposes dominate the reservoir water storage changes in EA, YR, and SW, particularly during or before rainy seasons. Our findings underscore the intricate interplay between natural and anthropogenic factors in shaping the reservoir water storage dynamics across China's diverse regions during the study period.

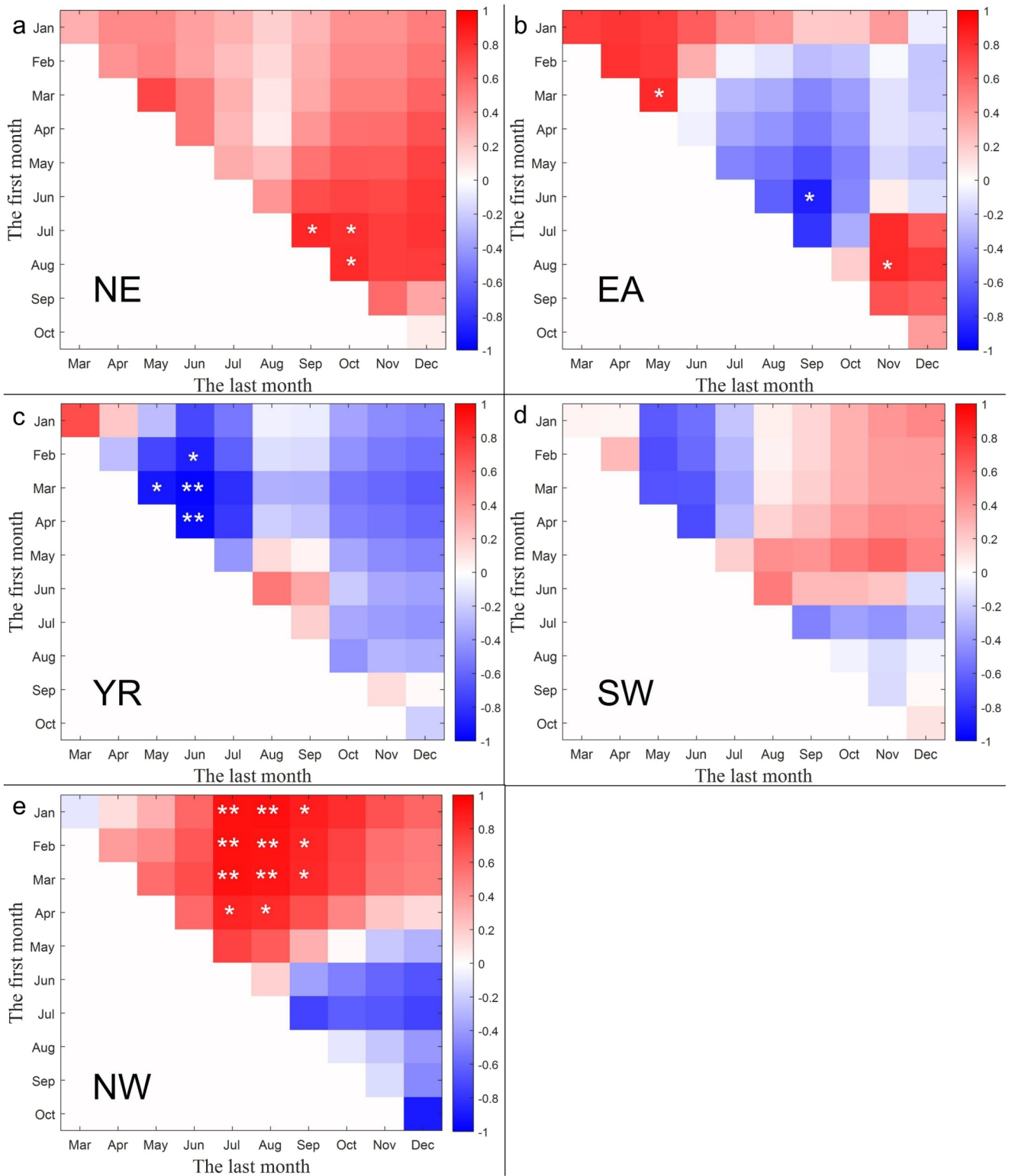


Figure 8.

5.3. Spatiotemporal Heterogeneity of the Threshold SAR Backscatter for Identifying Inundated/Dry Status in Reservoirs

Here, we present the seasonal variation of the relationship between the estimated inundation probability and the Sentinel-1 VV-polarized backscatter (γ^0) across the largest reservoirs in different regions of China. As shown in Figure 10, there are significant spatial and temporal variations in the threshold VV backscatter, and the seasonal variation pattern of the threshold VV backscatter differs among different reservoirs. This result reveals high spatiotemporal heterogeneity in the threshold Sentinel-1 SAR backscatter for identifying inundated or dry status in reservoirs, highlighting the importance of developing regional/reservoir- and monthly-specific machine learning models. Additionally, according to Figure 10, whether the JRC or GLAD-based inundation status identifications are used as the training target will only slightly alter the monthly VV backscatter thresholds in most reservoirs, suggesting that our method is generally robust and that the estimated threshold VV backscatter values are reliable.

5.4. Limitations and Prospects

While the integration of SAR with optical remote sensing in this study has facilitated the monthly monitoring of inundated areas at 721 large reservoirs across China, it is essential to acknowledge certain limitations. The quality of reservoir inundated area estimates can be influenced by the following factors: (a) Ice cover: freezing can increase SAR backscatters in reservoirs, leading to lower accuracies in the SVM models during cooler seasons, particularly in high-altitude or high-latitude regions like Northeast China (Figure 5); (b) Dry bare soil: dry and bare soils show low SAR backscatters, which are similar to those of surface water (Liang & Liu, 2020), contributing to lower accuracies in the SVM models during non-growing seasons, typically cooler seasons in China; and (c) Aquatic vegetation: the presence of emergent or floating aquatic vegetation in some reservoirs can also affect the accuracy of inundated area identifications, particularly in warmer seasons (Pu et al., 2022). According to Figure S12 in Supporting Information S1, when the GLAD and JRC data sets are respectively used as the training targets, approximately 4% and 7% of all 785 reservoirs have more than 1 month lacking high-accuracy SVM models during warmer seasons (May–October). In cooler seasons, the corresponding fractions are 10% and 16%, respectively. This result indicates that more reservoirs in China experience disturbances due to ice cover and dry bare soil compared to disturbances caused by aquatic vegetation.

To improve the quantity and quality of monthly inundated area retrieval, the integration of optical remote sensing data with higher temporal resolution (e.g., Moderate Resolution Imaging Spectroradiometer and Sentinel-2) can help distinguish between barren land and surface water on a monthly scale (Khandelwal et al., 2017; Tulbure et al., 2022). However, accurately differentiating frozen waters and near-shore aquatic vegetation from surrounding ice/snow and vegetation remains a challenge (Alsdorf et al., 2007). Utilizing more advanced machine learning techniques such as contextual complex Wishart classification (Goumehei et al., 2019) and deep convolutional neural networks (B. Liu et al., 2019) could be promising avenues for further enhancement.

On another note, the hypsometry relationship estimation in this study introduced more errors into the water storage change estimates compared to the inundated area retrieval (Figure 6 and Figure S9 in Supporting Information S1), primarily due to the limited availability of high-quality satellite altimetry records over most reservoirs. Notably, the hypsometry relationships of 59 out of 721 large reservoirs were not obtained. To reduce the rRMSE of reservoir water storage to below 20%, it is crucial to have adequate satellite altimetry data for nearly every reservoir (Figure 6d). Fortunately, this would be addressed by the newly launched Surface Water Ocean Topography (SWOT) mission.

SWOT carries the Ka-band interferometric SAR system “KaRIn,” which can provide 2D swath observations of surface water level at approximately 50 m resolution, a significant improvement over the nadir-pointing altimetry sensors (Durand et al., 2010; Morrow et al., 2019; Munier et al., 2015). SWOT enables frequent visits to surface

Figure 8. Correlation coefficients (CC) between reservoir water storage and accumulated natural inflow. This figure presents CC matrices representing the relationships between estimated reservoir water storage and accumulated natural inflow during different time periods, ranging from the “first month” to the “last month” within each year. The matrices are divided into five subfigures, each corresponding to a distinct region in China (see Figure 1). Significant positive correlations (colored in red) at the 95% confidence level are denoted by one asterisk, while highly significant positive correlations (colored in red) at the 99% confidence level are indicated by two asterisks. Similarly, significant negative correlations (colored in blue) at the 95% confidence level are marked with one asterisk, and highly significant negative correlations (colored in blue) at the 99% confidence level are represented by two asterisks.

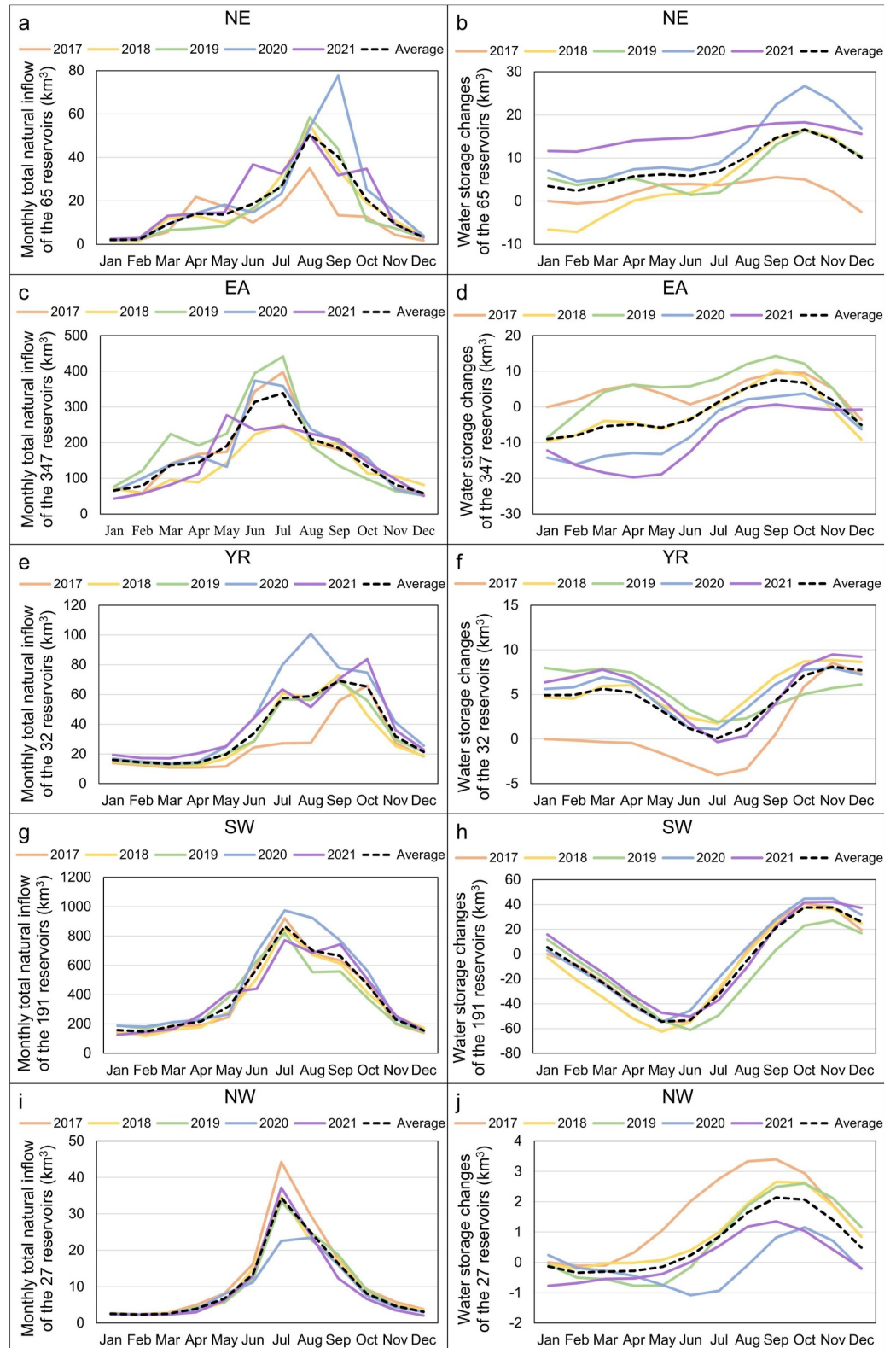


Figure 9. Seasonal variations of (a, c, e, g, i) natural inflow and (b, d, f, h, j) reservoir water storage in each year during 2017–2021 across different regions of China. The dashed lines represent the multi-year averaged seasonal variations. Regional classification in China is shown in Figure 1.

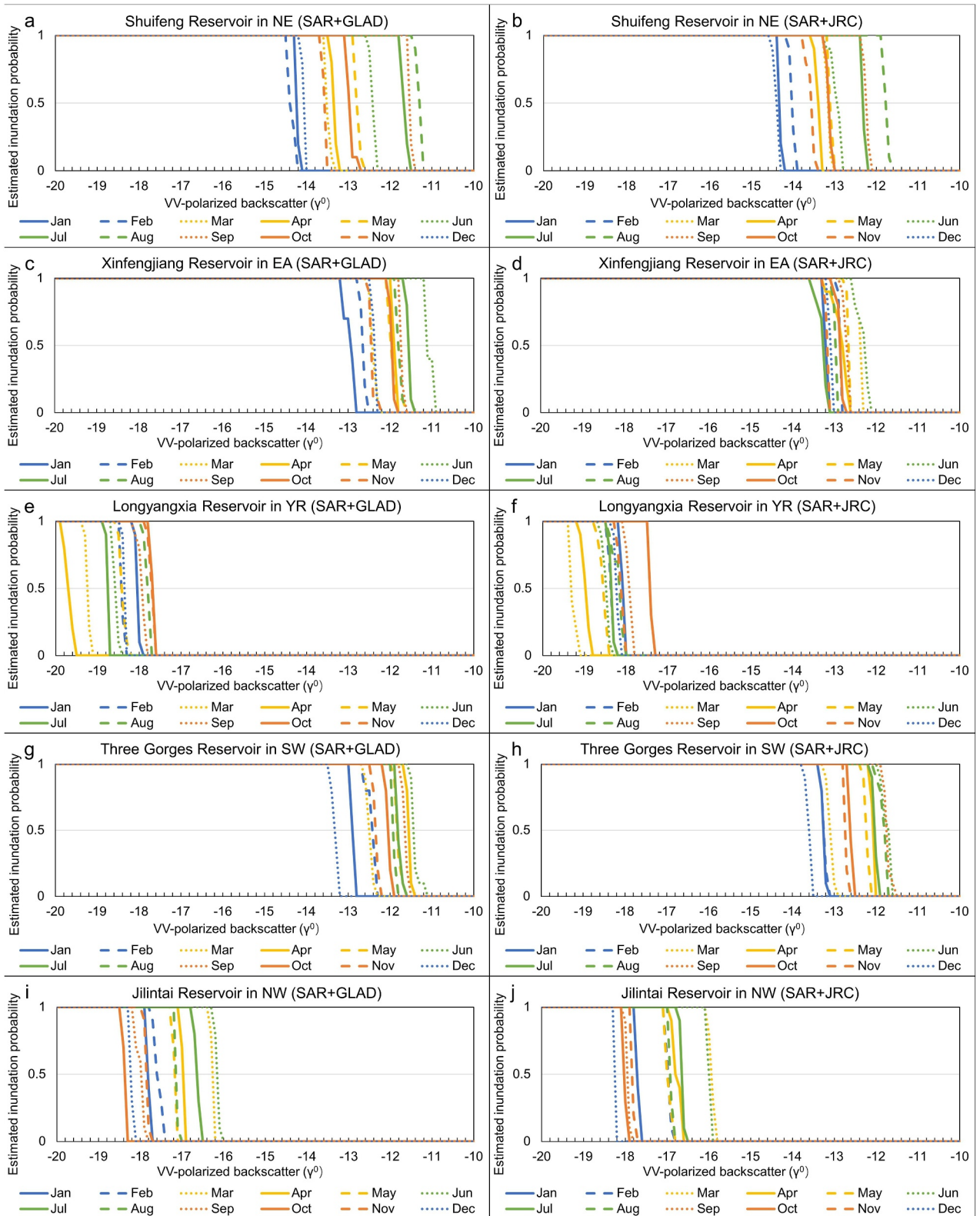


Figure 10. Seasonal variation of the relationship between the estimated inundation probability and the Vertical-vertical (VV)-polarized backscatter (γ^0) across the largest reservoirs in different regions of China. Synthetic aperture radar (SAR) + Joint Research Center (JRC) and SAR + Global Land Analysis and Discovery (GLAD) denote scenarios in which inundation status identifications based on the JRC and GLAD data sets were utilized as training targets, respectively.

water bodies on Earth, typically every 2–4 days, with a measurement error limited to only 10 cm (Biancamaria et al., 2010). Moreover, SWOT's capability to capture inundated extents from its images will be less affected by aquatic vegetation (Durand et al., 2010). Therefore, the integration of SWOT data in the near future promises to significantly enhance hypsometry relationship estimation and water storage change monitoring for lakes and reservoirs at large spatial scales.

Finally, some reservoirs, particularly those in the YR, may undergo silting and desilting processes (Zhang et al., 2021), causing changes in reservoir hypsometry relationships. Future studies should pay particular attention to hypsometry relationship estimation during different periods for these reservoirs to provide a more accurate understanding of water storage changes.

6. Conclusion

In this study, we have significantly enhanced the monthly monitoring of inundated areas and water storage changes in large reservoirs across China for the period 2017–2021, leveraging the potential of multisource remote sensing data. We derived monthly inundated areas for 721 out of 785 large reservoirs in China, and estimated monthly water storage changes at 662 reservoirs, encompassing a remarkable 93% of the total storage capacity of all large reservoirs in China.

The Spearman CC between our estimated monthly inundated areas and the measured monthly mean water levels at 80 large reservoirs reached 0.85 (mean) ± 0.13 (standard deviation), improved compared to existing studies. Furthermore, we scrutinized the validation against in-situ reservoir water storage, revealing an impressive R^2 of 0.79 ± 0.18 and rRMSE of $21\% \pm 14\%$ for our estimates of monthly reservoir water storage changes.

Our findings unveiled compelling insights into the seasonal dynamics of reservoir water storage across diverse regions of China. We observed a consistent pattern of increasing water storage from May/June to November, followed by a decline in winter and spring, primarily influenced by the stable seasonal variations in Southwest China. However, other geographical regions displayed notably distinct seasonal variation patterns, which could also undergo significant year-to-year variations. Our analysis further revealed that shallower reservoirs in China were experiencing a decline, while deeper reservoirs exhibited expansion trends, leading to divergent trajectories in the inundated area and water storage of large reservoirs. Specifically, Northeast China, the YR, and Southwest China, where deeper reservoirs predominate, witnessed a significant rise in total water storage, whereas the shallower reservoir-dominated Eastern China and Northwest China reported declining water storage.

Our investigation into the influences on reservoir water storage dynamics illuminated distinct drivers across different regions. In Northeast and Northwest China, variations in natural inflow were found to exert substantial influence on both inter-annual and intra-annual reservoir water storage fluctuations. Conversely, anthropogenic factors, particularly the regulation of outflow for flood control, hydropower generation, and ice-jam prevention, played a dominant role in shaping reservoir water storage dynamics in the YR, Eastern China, and Southwest China.

In conclusion, our study represents a significant advancement in the monitoring and understanding of large reservoir dynamics across China. The robust data sets generated, along with the insights gained, offer valuable contributions to reservoir management, hydrological modeling, and the sustainable utilization of these critical water resources in a rapidly changing world.

Conflict of Interest

The authors declare no conflicts of interest relevant to this study.

Data Availability Statement

We are committed to making our calibrated geospatial data set covering all large reservoirs in China, along with the estimated monthly inundated areas for 721 reservoirs and monthly water storage changes for 662 reservoirs, openly accessible to the scientific community. These data sets have been deposited on PANGAEA (<https://doi.pangaea.de/10.1594/PANGAEA.961148>) for ease of access and utilization by researchers and stakeholders.

The data and codes utilized in this study have been sourced from publicly available data sets. Details are as follows:

The Joint Research Center (JRC)'s global surface dynamics data set (Pekel et al., 2016) is available at: <https://global-surface-water.appspot.com/download>, or https://developers.google.cn/earth-engine/datasets/catalog/JRC_GSW1_4_YearlyHistory?hl=en and https://developers.google.cn/earth-engine/datasets/catalog/JRC_GSW1_4_MonthlyHistory?hl=en.

The Global Land Analysis and Discovery (GLAD)'s global surface dynamics data set (Pickens et al., 2020) is available at: <https://glad.umd.edu/dataset/global-surface-water-dynamics>.

The China Reservoir Data set (CRD) data set (Song et al., 2022) can be accessed at: <https://doi.org/10.5281/zenodo.6984619>.

The processed Sentinel-1 SAR data are available on Google Earth Engine (Gorelick et al., 2017) at: https://developers.google.cn/earth-engine/datasets/catalog/COPERNICUS_S1_GRD?hl=en.

The CryoSat-2 Level 2 Geophysical Data Record (GDR) data is provided by European Space Agency (ESA, 2019), and can be accessed at: <ftp://science-pds.cryosat.esa.int/>.

ICESat-2 L3A Along Track Inland Surface Water Data (ATL 13) V005 product (Jasinski et al., 2021) is available at: <https://nsidc.org/data/atl13/versions/5>.

GEDI L2A Raster Canopy Top Height Version 2 (Dubayah et al., 2021) can be accessed on Google Earth Engine: https://developers.google.cn/earth-engine/datasets/catalog/LARSE_GEDI_GEDI02_A_002_MONTHLY?hl=en.

Global Reservoirs and Lakes Monitor (G-REALM) altimetry data (Birkett et al., 2011, 2019) can be downloaded from: https://ipad.fas.usda.gov/cropexplorer/global_reservoir/.

The Database for Hydrological Time Series of Inland Waters (DAHITI) (Schwatke et al., 2015) is available at: <https://dahiti.dgfi.tum.de/en/>.

The Le laboratoire d'études en géophysique et océanographie spatiales (LEGOS) Hydroweb data (Crétaux et al., 2011) is available at: <https://hydroweb.theia-land.fr/>.

The China Reservoir Water Level Data set (Shen et al., 2022) can be accessed at: <https://doi.org/10.5281/zenodo.7251283>.

The Multi-Error-Removed Improved-Terrain (MERIT) DEM data (Yamazaki et al., 2017) is available at: http://hydro.iis.u-tokyo.ac.jp/~yamada/MERIT_DEM/ or https://developers.google.cn/earth-engine/datasets/catalog/MERIT_DEM_v1_0_3.

The Copernicus DEM data (ESA, 2021) is from: https://developers.google.com/earth-engine/datasets/catalog/COPERNICUS_DEM_GLO30 or <https://portal.opentopography.org/raster?opentopoID=OTSDEM.032021.4326.3>.

The SRTM Water Body Data Shapefiles and Raster Files (SRTMSWBD v003) (NASA, 2013) is available from: <https://lpdaac.usgs.gov/products/srtmswbdv003/>.

The in-situ reservoir water level and water storage records were obtained from the Ministry of Water Resources-National Hydrological Information Center at: http://xxfb.mwr.cn/sq_dxsk.html (MWR-NHIC, 2023), the Yellow River Conservancy Commission at: <http://61.163.88.227:8006/hwsq.aspx> (YRCC, 2023), and various provincial hydrological information websites, including: <http://yzt.hnswkj.com:9090/#/>, <http://www.schw.com/article/45>, and <http://113.57.190.228:8001/web/Report/BigMSKReport>. For some websites, register is required to see the data. And, you might need to check and download the data every day to composite a time series.

The Global Lake Evaporation Volume data set was developed in G. Zhao et al. (2022), and can be accessed at: <https://zenodo.org/record/4646621>.

The Global Reservoir Surface Area Data set (GRSAD) was developed in G. Zhao and Gao (2018), and can be accessed at: <https://dataverse.tdl.org/dataset.xhtml?persistentId=doi:10.18738/T8/DF80WG>.

Global Flood Awareness System (GloFAS) version 4.0 data set (Grimaldi et al., 2022b) can be accessed at: <https://cds.climate.copernicus.eu/cdsapp#!/dataset/cems-glofas-historical?tab=overview>.

The MATLAB code for Shape Language Modeling (SLM) algorithm (D'Errico, 2023) can be downloaded from: <https://ww2.mathworks.cn/matlabcentral/fileexchange/24443-slm-shape-language-modeling?requestedDomain=zh>.

Acknowledgments

This study was jointly supported by the National Natural Science Foundation of China (Grant 52325901) and the Second Tibetan Plateau Scientific Expedition and Research (STEP) program (2019QZKK0105). Editors and reviewers' comments are highly appreciated.

References

- Alfieri, L., Lorini, V., Hirpa, F. A., Harrigan, S., Zsoter, E., Prudhomme, C., & Salamon, P. (2020). A global streamflow reanalysis for 1980–2018. *Journal of Hydrology X*, 6, 100049. <https://doi.org/10.1016/j.hydroa.2019.100049>
- Alsdorf, D. E., Rodriguez, E., & Lettenmaier, D. P. (2007). Measuring surface water from space. *Reviews of Geophysics*, 45(2), RG2002. <https://doi.org/10.1029/2006RG000197>
- Aristizabal, F., Judge, J., & Monsivais-Huetero, A. (2020). High-resolution inundation mapping for heterogeneous land covers with synthetic aperture radar and terrain data. *Remote Sensing*, 12(6), 900. <https://doi.org/10.3390/rs12060900>
- Avisse, N., Tilmant, A., Müller, M. F., & Zhang, H. (2017). Monitoring small reservoirs' storage with satellite remote sensing in inaccessible areas. *Hydrology and Earth System Sciences*, 21(12), 6445–6459. <https://doi.org/10.5194/hess-21-6445-2017>
- Bastarrica, A., Chuvieco, E., & Martín, M. P. (2011). Mapping burned areas from Landsat TM/ETM+ data with a two-phase algorithm: Balancing omission and commission errors. *Remote Sensing of Environment*, 115(4), 1003–1012. <https://doi.org/10.1016/j.rse.2010.12.005>
- Biancamaria, S., Andreadis, K. M., Durand, M., Clark, E. A., Rodriguez, E., Mognard, N. M., et al. (2010). Preliminary characterization of SWOT hydrology error budget and global capabilities. *IEEE Journal of Selected Topics in Applied Earth Observations and Remote Sensing*, 3(1), 6–19. <https://doi.org/10.1109/jstars.2009.2034614>
- Biemans, H., Haddeland, I., Kabat, P., Ludwig, F., Hutjes, R. W. A., Heinke, J., et al. (2011). Impact of reservoirs on river discharge and irrigation water supply during the 20th century. *Water Resources Research*, 47(3), W03509. <https://doi.org/10.1029/2009WR008929>
- Birkett, C., Reynolds, C., Beckley, B., & Doorn, B. (2011). From research to operations: The USDA Global Reservoir and Lake Monitor. In S. Vignudelli, A. G. Kostianoy, P. Cipollini, & J. Benveniste (Eds.), *Coastal altimetry* (pp. 19–50). Springer Berlin Heidelberg.
- Birkett, C., Ricko, M., & Yang, X. (2019). Pre SWOT hydrology global lake/reservoir surface inland water height GREATM V.2. Retrieved from https://podaac.jpl.nasa.gov/dataset/PRESWOT_HYDRO_L2_GREALM_LAKE_HEIGHT_V2
- Bonnema, M., David, C. H., Frasson, R. P. D. M., Oaida, C., & Yun, S.-H. (2022). The global surface area variations of lakes and reservoirs as seen from satellite remote sensing. *Geophysical Research Letters*, 49(15), e2022GL098987. <https://doi.org/10.1029/2022GL098987>
- Chang, C.-C., & Lin, C.-J. (2011). LIBSVM: A library for support vector machines. *ACM Transactions on Intelligent Systems and Technology*, 2(3), 1–27. <https://doi.org/10.1145/1961189.1961199>
- Chang, J., Wang, X., Li, Y., & Wang, Y. (2016). Ice regime variation impacted by reservoir operation in the Ning-Meng reach of the Yellow River. *Natural Hazards*, 80(2), 1015–1030. <https://doi.org/10.1007/s11069-015-2010-5>
- Cooley, S. W., Ryan, J. C., & Smith, L. C. (2021). Human alteration of global surface water storage variability. *Nature*, 591(7848), 78–81. <https://doi.org/10.1038/s41586-021-03262-3>
- Crétau, J. F., Arsen, A., Calmant, S., Kouraev, A., Vuglinski, V., Bergé-Nguyen, M., et al. (2011). SOLS: A lake database to monitor in the Near Real Time water level and storage variations from remote sensing data. *Advances in Space Research*, 47(9), 1497–1507. <https://doi.org/10.1016/j.asr.2011.01.004>
- Dai, K., Chen, C., Shi, X., Wu, M., Feng, W., Xu, Q., et al. (2023). Dynamic landslides susceptibility evaluation in Baihetan Dam area during extensive impoundment by integrating geological model and InSAR observations. *International Journal of Applied Earth Observation and Geoinformation*, 116, 103157. <https://doi.org/10.1016/j.jag.2022.103157>
- D'Errico, J. (2023). SLM - Shape Language Modeling. Retrieved from <https://www.mathworks.com/matlabcentral/fileexchange/24443-slm-shape-language-modeling>
- Do, P., Tian, F., Zhu, T., Zohidov, B., Ni, G., Lu, H., & Liu, H. (2020). Exploring synergies in the water-food-energy nexus by using an integrated hydro-economic optimization model for the Lancang-Mekong River basin. *Science of the Total Environment*, 728, 137996. <https://doi.org/10.1016/j.scitotenv.2020.137996>
- Donchyts, G., Winsemius, H., Baart, F., Dahm, R., Schellekens, J., Gorelick, N., et al. (2022). High-resolution surface water dynamics in Earth's small and medium-sized reservoirs. *Scientific Reports*, 12(1), 13776. <https://doi.org/10.1038/s41598-022-17074-6>
- Dong, N., Wei, J., Yang, M., Yan, D., Yang, C., Gao, H., et al. (2022). Model estimates of China's terrestrial water storage variation due to reservoir operation. *Water Resources Research*, 58(6), e2021WR031787. <https://doi.org/10.1029/2021WR031787>
- Druce, D., Tong, X., Lei, X., Guo, T., Kittel, C. M. M., Grogan, K., & Tottrup, C. (2021). An optical and SAR based fusion approach for mapping surface water dynamics over Mainland China. *Remote Sensing*, 13(9), 1663. <https://doi.org/10.3390/rs13091663>
- Dubayah, R., Hofton, M., Blair, J., Armston, J., Tang, H., & Luthcke, S. (2021). GEDI L2A elevation and height metrics data global footprint level V002 [Dataset]. https://doi.org/10.5067/GEDI/GEDI02_A_002
- Durand, M., Fu, L. L., Lettenmaier, D. P., Alsdorf, D. E., Rodriguez, E., & Esteban-Fernandez, D. (2010). The surface water and ocean topography mission: Observing terrestrial surface water and oceanic submesoscale eddies. *Proceedings of the IEEE*, 98(5), 766–779. <https://doi.org/10.1109/jproc.2010.2043031>
- ESA. (2019). GDR precise orbit. Baseline D. <https://doi.org/10.5270/CR2-he6wflr>
- ESA. (2021). Copernicus Global Digital Elevation Model. <https://doi.org/10.5069/G9028PQB>
- Fang, Y., & Deng, W. (2011). The critical scale and section management of cascade hydropower exploitation in Southwestern China. *Energy*, 36(10), 5944–5953. <https://doi.org/10.1016/j.energy.2011.08.022>
- Fayad, I., Baghdadi, N., Bailly, J. S., Frappart, F., & Zribi, M. (2020). Analysis of GEDI elevation data accuracy for inland waterbodies altimetry. *Remote Sensing*, 12(17), 2714. <https://doi.org/10.3390/rs12172714>
- Feng, Z., Zheng, X., Li, L., Li, B., Chen, S., Guo, T., et al. (2021). Dynamic Cosine method for normalizing incidence angle effect on C-band radar backscattering coefficient for maize canopies based on NDVI. *Remote Sensing*, 13(15), 2856. <https://doi.org/10.3390/rs13152856>
- Gorelick, N., Hancher, M., Dixon, M., Ilyushchenko, S., Thau, D., & Moore, R. (2017). Google Earth Engine: Planetary-scale geospatial analysis for everyone. *Remote Sensing of Environment*, 202, 18–27. <https://doi.org/10.1016/j.rse.2017.06.031>
- Gou, J., Miao, C., Samaniego, L., Xiao, M., Wu, J., & Guo, X. (2021). CNRD v1.0: A high-quality natural runoff dataset for hydrological and climate studies in China. *Bulletin of the American Meteorological Society*, 102(5), E929–E947. <https://doi.org/10.1175/bams-d-20-0094.1>

- Goumehei, E., Tolpekin, V., Stein, A., & Yan, W. (2019). Surface water body detection in polarimetric SAR data using contextual complex Wishart classification. *Water Resources Research*, 55(8), 7047–7059. <https://doi.org/10.1029/2019WR025192>
- Grill, G., Lehner, B., Thieme, M., Geenen, B., Tickner, D., Antonelli, F., et al. (2019). Mapping the world's free-flowing rivers. *Nature*, 569(7755), 215–221. <https://doi.org/10.1038/s41586-019-1111-9>
- Grimaldi, S., Salamon, P., Disperati, J., Zsoter, E., Russo, C., Ramos, A., et al. (2022a). GloFAS v4.0 hydrological reanalysis. Retrieved from <http://data.europa.eu/89h/f96b7a19-0133-4105-a879-0536991ca9c5>
- Grimaldi, S., Salamon, P., Disperati, J., Zsoter, E., Russo, C., Ramos, A., et al. (2022b). River discharge and related historical data from the Global Flood Awareness System. v4.0. Retrieved from <https://cds.climate.copernicus.eu/cdsapp#!/dataset/cems-glofas-historical>
- Gulácsi, A., & Kovács, F. (2020). Sentinel-1-imagery-based high-resolution water cover detection on wetlands, aided by Google Earth Engine. *Remote Sensing*, 12(10), 1614. <https://doi.org/10.3390/rs12101614>
- Han, Z., Long, D., Huang, Q., Li, X., Zhao, F., & Wang, J. (2020). Improving reservoir outflow estimation for ungauged basins using satellite observations and a hydrological model. *Water Resources Research*, 56(9), e2020WR027590. <https://doi.org/10.1029/2020WR027590>
- Harrigan, S., Zsoter, E., Alfieri, L., Prudhomme, C., Salamon, P., Wetterhall, F., et al. (2020). GloFAS-ERA5 operational global river discharge reanalysis 1979–present. *Earth System Science Data*, 12(3), 2043–2060. <https://doi.org/10.5194/essd-12-2043-2020>
- Hird, J. N., DeLancey, E. R., McDermid, G. J., & Kariyeva, J. (2017). Google Earth Engine, Open-access satellite data, and machine learning in support of large-area probabilistic wetland mapping. *Remote Sensing*, 9(12), 1315. <https://doi.org/10.3390/rs9121315>
- Hou, J., van Dijk, A. I. J. M., Beck, H. E., Renzullo, L. J., & Wada, Y. (2022). Remotely sensed reservoir water storage dynamics (1984–2015) and the influence of climate variability and management at a global scale. *Hydrology and Earth System Sciences*, 26(14), 3785–3803. <https://doi.org/10.5194/hess-26-3785-2022>
- Intralawan, A., Wood, D., Frankel, R., Costanza, R., & Kubiszewski, I. (2018). Tradeoff analysis between electricity generation and ecosystem services in the Lower Mekong Basin. *Ecosystem Services*, 30, 27–35. <https://doi.org/10.1016/j.ecoser.2018.01.007>
- Jasinski, M. F., Stoll, J. D., Hancock, D., Robbins, J., Nattala, J., Morison, J., et al. (2021). ATLAS/ICESat-2 L3A along track inland surface water data, Version 5. Retrieved from <https://nsidc.org/data/atl13/versions/5>
- Jiang, L., Nielsen, K., Andersen, O. B., & Bauer-Gottwein, P. (2017). CryoSat-2 radar altimetry for monitoring freshwater resources of China. *Remote Sensing of Environment*, 200, 125–139. <https://doi.org/10.1016/j.rse.2017.08.015>
- Jiang, Z., Jiang, W., Ling, Z., Wang, X., Peng, K., & Wang, C. (2021). Surface water extraction and dynamic analysis of Baiyangdian Lake based on the Google Earth Engine platform using Sentinel-1 for reporting SDG 6.6.1 indicators. *Water*, 13(2), 138. <https://doi.org/10.3390/w13020138>
- Keller, P. S., Marcé, R., Obrador, B., & Koschorreck, M. (2021). Global carbon budget of reservoirs is overturned by the quantification of drawdown areas. *Nature Geoscience*, 14(6), 402–408. <https://doi.org/10.1038/s41561-021-00734-z>
- Khandelwal, A., Karpatne, A., Marlier, M. E., Kim, J., Lettenmaier, D. P., & Kumar, V. (2017). An approach for global monitoring of surface water extent variations in reservoirs using MODIS data. *Remote Sensing of Environment*, 202, 113–128. <https://doi.org/10.1016/j.rse.2017.05.039>
- Khazaei, B., Read, L. K., Casali, M., Sampson, K. M., & Yates, D. N. (2022). GLOBathy, the global lakes bathymetry dataset. *Scientific Data*, 9(1), 36. <https://doi.org/10.1038/s41597-022-01132-9>
- Konapala, G., Kumar, S. V., & Khalique Ahmad, S. (2021). Exploring Sentinel-1 and Sentinel-2 diversity for flood inundation mapping using deep learning. *ISPRS Journal of Photogrammetry and Remote Sensing*, 180, 163–173. <https://doi.org/10.1016/j.isprsjprs.2021.08.016>
- Lee, J. S., Wen, J. H., Ainsworth, T. L., Chen, K. S., & Chen, A. J. (2009). Improved sigma filter for speckle filtering of SAR imagery. *IEEE Transactions on Geoscience and Remote Sensing*, 47(1), 202–213. <https://doi.org/10.1109/TGRS.2008.2002881>
- Lehner, B., Liermann, C. R., Revenga, C., Vörösmarty, C., Fekete, B., Crouzet, P., et al. (2011). High-resolution mapping of the world's reservoirs and dams for sustainable river-flow management. *Frontiers in Ecology and the Environment*, 9(9), 494–502. <https://doi.org/10.1890/100125>
- Lehner, B., Reidy Liermann, C., Revenga, C., Vörösmarty, C., Fekete, B., & Crouzet, P. (2019). Global reservoir and dam database, version 1.3. (GRanDv1.3): reservoirs. Retrieved from <https://www.globaldamwatch.org/grand>
- Li, S., Li, J., Du, W., Liu, S., Wang, H., & Jin, J. (2024). Combining Satellite images and the hydraulic engineering archive to map the processes of reservoir construction in Xinjiang. *Remote Sensing*, 16(2), 328. <https://doi.org/10.3390/rs16020328>
- Li, S., Tan, H., Liu, Z., Zhou, Z., Liu, Y., Zhang, W., et al. (2018). Mapping high mountain lakes using space-borne near-nadir SAR observations. *Remote Sensing*, 10(9), 1418. <https://doi.org/10.3390/rs10091418>
- Li, X., Long, D., Huang, Q., Han, P., Zhao, F., & Wada, Y. (2019). High-temporal-resolution water level and storage change data sets for lakes on the Tibetan Plateau during 2000–2017 using multiple altimetric missions and Landsat-derived lake shoreline positions. *Earth System Science Data*, 11(4), 1603–1627. <https://doi.org/10.5194/essd-11-1603-2019>
- Li, Y., Niu, Z., Xu, Z., & Yan, X. (2020). Construction of high spatial-temporal water body dataset in China based on Sentinel-1 archives and GEE. *Remote Sensing*, 12(15), 2413. <https://doi.org/10.3390/rs12152413>
- Liang, J., & Liu, D. (2020). A local thresholding approach to flood water delineation using Sentinel-1 SAR imagery. *ISPRS Journal of Photogrammetry and Remote Sensing*, 159, 53–62. <https://doi.org/10.1016/j.isprsjprs.2019.10.017>
- Liu, B., Li, X., & Zheng, G. (2019). Coastal inundation mapping from bitemporal and dual-polarization SAR imagery based on deep convolutional neural networks. *Journal of Geophysical Research: Oceans*, 124(12), 9101–9113. <https://doi.org/10.1029/2019JC015577>
- Liu, P., Li, L., Guo, S., Xiong, L., Zhang, W., Zhang, J., & Xu, C.-Y. (2015). Optimal design of seasonal flood limited water levels and its application for the Three Gorges Reservoir. *Journal of Hydrology*, 527, 1045–1053. <https://doi.org/10.1016/j.jhydrol.2015.05.055>
- Liu, Z., Yao, Z., & Wang, R. (2019). Evaluation and validation of CryoSat-2-derived water levels using in situ lake data from China. *Remote Sensing*, 11(8), 899. <https://doi.org/10.3390/rs11080899>
- Magruder, L., Neuenschwander, A., & Klotz, B. (2021). Digital terrain model elevation corrections using space-based imagery and ICESat-2 laser altimetry. *Remote Sensing of Environment*, 264, 112621. <https://doi.org/10.1016/j.rse.2021.112621>
- Markus, T., Neumann, T., Martino, A., Abdalati, W., Brunt, K., Csatho, B., et al. (2017). The Ice, Cloud, and land Elevation Satellite-2 (ICESat-2): Science requirements, concept, and implementation. *Remote Sensing of Environment*, 190, 260–273. <https://doi.org/10.1016/j.rse.2016.12.029>
- Messenger, M. L., Lehner, B., Grill, G., Nedeva, I., & Schmitt, O. (2016). Estimating the volume and age of water stored in global lakes using a geostatistical approach. *Nature Communications*, 7(1), 13603. <https://doi.org/10.1038/ncomms13603>
- Morrow, R., Fu, L.-L., Arduhin, F., Benkiran, M., Chapron, B., Cosme, E., et al. (2019). Global observations of fine-scale ocean surface topography with the Surface Water and Ocean Topography (SWOT) mission. *Frontiers in Marine Science*, 6, 232. Review. <https://doi.org/10.3389/fmars.2019.00232>
- Mountrakis, G., Im, J., & Ogole, C. (2011). Support vector machines in remote sensing: A review. *ISPRS Journal of Photogrammetry and Remote Sensing*, 66(3), 247–259. <https://doi.org/10.1016/j.isprsjprs.2010.11.001>

- Mulligan, M., van Soesbergen, A., & Sáenz, L. (2020). GOODD, a global dataset of more than 38,000 georeferenced dams. *Scientific Data*, 7(1), 31. <https://doi.org/10.1038/s41597-020-0362-5>
- Mullissa, A., Vollrath, A., Odongo-Braun, C., Slagter, B., Balling, J., Gou, Y., et al. (2021). Sentinel-1 SAR backscatter analysis ready data preparation in Google Earth Engine. *Remote Sensing*, 13(10), 1954. <https://doi.org/10.3390/rs13101954>
- Munier, S., Polebistki, A., Brown, C., Belaud, G., & Lettenmaier, D. P. (2015). SWOT data assimilation for operational reservoir management on the upper Niger River Basin. *Water Resources Research*, 51(1), 554–575. <https://doi.org/10.1002/2014WR016157>
- MWR-NHIC. (2023). Retrieved from http://xxfb.mwr.cn/sq_dxsk.html
- NASA. (2013). NASA shuttle radar topography mission water body data Shapefiles & Raster files. <https://doi.org/10.5067/MEASURES/SRTM/SRTMSWBD.003>
- Otsu, N. (1979). A threshold selection method from gray-level histograms. *IEEE Transactions on Systems, Man, and Cybernetics*, 9(1), 62–66. <https://doi.org/10.1109/TSMC.1979.4310076>
- Pekel, J.-F., Cottam, A., Gorelick, N., & Belward, A. S. (2016). High-resolution mapping of global surface water and its long-term changes. *Nature*, 540(7633), 418–422. <https://doi.org/10.1038/nature20584>
- Pickens, A. H., Hansen, M. C., Hancher, M., Stehman, S. V., Tyukavina, A., Potapov, P., et al. (2020). Mapping and sampling to characterize global inland water dynamics from 1999 to 2018 with full Landsat time-series. *Remote Sensing of Environment*, 243, 111792. <https://doi.org/10.1016/j.rse.2020.111792>
- Pu, J., Song, K., Lv, Y., Liu, G., Fang, C., Hou, J., & Wen, Z. (2022). Distinguishing algal blooms from aquatic vegetation in Chinese lakes using Sentinel 2 image. *Remote Sensing*, 14(9), 1988. <https://doi.org/10.3390/rs14091988>
- Qi, W., Feng, L., Yang, H., & Liu, J. (2021). Spring and summer potential flood risk in Northeast China. *Journal of Hydrology: Regional Studies*, 38, 100951. <https://doi.org/10.1016/j.ejrh.2021.100951>
- Ruan, Y., Zhang, X., Xin, Q., Qiu, Y., & Sun, Y. (2020). Prediction and analysis of lake ice phenology dynamics under future climate scenarios across the Inner Tibetan Plateau. *Journal of Geophysical Research: Atmospheres*, 125(23), e2020JD033082. <https://doi.org/10.1029/2020JD033082>
- Schwatke, C., Dettmering, D., Bosch, W., & Seitz, F. (2015). DAHITI – An innovative approach for estimating water level time series over inland waters using multi-mission satellite altimetry. *Hydrology and Earth System Sciences*, 19(10), 4345–4364. <https://doi.org/10.5194/hess-19-4345-2015>
- Shamshiri, R., Eide, E., & Høyland, K. V. (2022). Spatio-temporal distribution of sea-ice thickness using a machine learning approach with Google Earth Engine and Sentinel-1 GRD data. *Remote Sensing of Environment*, 270, 112851. <https://doi.org/10.1016/j.rse.2021.112851>
- Shen, Y., Liu, D., Jiang, L., Nielsen, K., Yin, J., Liu, J., & Bauer-Gottwein, P. (2022). High-resolution water level and storage variation datasets for 338 reservoirs in China during 2010–2021. *Earth System Science Data*, 14(12), 5671–5694. <https://doi.org/10.5194/essd-14-5671-2022>
- Shen, Y., Nielsen, K., Revel, M., Liu, D., & Yamazaki, D. (2023). Res-CN (Reservoir dataset in China): Hydrometeorological time series and landscape attributes across 3254 Chinese reservoirs. *Earth System Science Data*, 15(7), 2781–2808. <https://doi.org/10.5194/essd-15-2781-2023>
- Small, D. (2011). Flattening gamma: Radiometric terrain correction for SAR imagery. *IEEE Transactions on Geoscience and Remote Sensing*, 49(8), 3081–3093. <https://doi.org/10.1109/tgrs.2011.2120616>
- Song, C., Fan, C., Zhu, J., Wang, J., Sheng, Y., Liu, K., et al. (2022). A comprehensive geospatial database of nearly 100000 reservoirs in China. *Earth System Science Data*, 14(9), 4017–4034. <https://doi.org/10.5194/essd-14-4017-2022>
- Soued, C., Harrison, J. A., Mercier-Blais, S., & Prairie, Y. T. (2022). Reservoir CO₂ and CH₄ emissions and their climate impact over the period 1900–2060. *Nature Geoscience*, 15(9), 700–705. <https://doi.org/10.1038/s41561-022-01004-2>
- Souza, W. D., Reis, L. G., Ruiz-Armenteros, A. M., Veleda, D., Ribeiro Neto, A., Fragoso, C. R., Jr., et al. (2022). Analysis of environmental and atmospheric influences in the use of SAR and optical imagery from Sentinel-1, Landsat-8, and Sentinel-2 in the operational monitoring of reservoir water level. *Remote Sensing*, 14(9), 2218. <https://doi.org/10.3390/rs14092218>
- Tang, H., Lu, S., Ali Baig, M. H., Li, M., Fang, C., & Wang, Y. (2022). Large-scale surface water mapping based on Landsat and Sentinel-1 images. *Water*, 14(9), 1454. <https://doi.org/10.3390/w14091454>
- Taube, C. M. (2000). Chapter 12: Three methods for computing the volume of a lake. In J. C. Schneider (Ed.), *Manual of fisheries survey methods II: With periodic updates*. Michigan Department of Natural Resources.
- Tulbure, M. G., Broich, M., Perin, V., Gaines, M., Ju, J., Stehman, S. V., et al. (2022). Can we detect more ephemeral floods with higher density harmonized Landsat Sentinel 2 data compared to Landsat 8 alone? *ISPRS Journal of Photogrammetry and Remote Sensing*, 185, 232–246. <https://doi.org/10.1016/j.isprsjprs.2022.01.021>
- Vollrath, A., Mullissa, A., & Reiche, J. (2020). Angular-based radiometric slope correction for Sentinel-1 on Google Earth Engine. *Remote Sensing*, 12(11), 1867. <https://doi.org/10.3390/rs12111867>
- Wang, X., de Linage, C., Famiglietti, J., & Zender, C. S. (2011). Gravity Recovery and Climate Experiment (GRACE) detection of water storage changes in the Three Gorges Reservoir of China and comparison with in situ measurements. *Water Resources Research*, 47(12), W12502. <https://doi.org/10.1029/2011WR010534>
- Wang, Y., Long, D., & Li, X. (2023). High-temporal-resolution monitoring of reservoir water storage of the Lancang-Mekong River. *Remote Sensing of Environment*, 292, 113575. <https://doi.org/10.1016/j.rse.2023.113575>
- Wong, T. T., & Yeh, P. Y. (2020). Reliable accuracy estimates from k-fold cross validation. *IEEE Transactions on Knowledge and Data Engineering*, 32(8), 1586–1594. <https://doi.org/10.1109/tkde.2019.2912815>
- Xiao, C., Li, P., Feng, Z., & Wu, X. (2018). Spatio-temporal differences in cloud cover of Landsat-8 OLI observations across China during 2013–2016. *Journal of Geographical Sciences*, 28(4), 429–444. <https://doi.org/10.1007/s11442-018-1482-0>
- Yamazaki, D., Ikeshima, D., Tawatari, R., Yamaguchi, T., O'Loughlin, F., Neal, J. C., et al. (2017). A high-accuracy map of global terrain elevations. *Geophysical Research Letters*, 44(11), 5844–5853. <https://doi.org/10.1002/2017GL072874>
- Yang, L., Yang, Y., Villarini, G., Li, X., Hu, H., Wang, L., et al. (2021). Climate more important for Chinese flood changes than reservoirs and land use. *Geophysical Research Letters*, 48(11), e2021GL093061. <https://doi.org/10.1029/2021GL093061>
- Yang, Q., Song, K., Wen, Z., Hao, X., & Fang, C. (2019). Recent trends of ice phenology for eight large lakes using MODIS products in Northeast China. *International Journal of Remote Sensing*, 40(14), 5388–5410. <https://doi.org/10.1080/01431161.2019.1579939>
- Yang, X., & Lu, X. (2014). Drastic change in China's lakes and reservoirs over the past decades. *Scientific Reports*, 4(1), 6041. <https://doi.org/10.1038/srep06041>
- Yang, X., Zhang, M., He, X., Ren, L., Pan, M., Yu, X., et al. (2020). Contrasting influences of human activities on hydrological drought regimes over China based on high-resolution simulations. *Water Resources Research*, 56(6), e2019WR025843. <https://doi.org/10.1029/2019WR025843>
- YRCC. (2023). Retrieved from <http://61.163.88.227:8006/hwsq.aspx>

- Yu, Y., Yu, R., Chen, X., Yu, G., Gan, M., & Disse, M. (2017). Agricultural water allocation strategies along the oasis of Tarim River in Northwest China. *Agricultural Water Management*, *187*, 24–36. <https://doi.org/10.1016/j.agwat.2017.03.021>
- Yuan, X., Zhang, Y., Liu, H., Xiong, S., Li, B., & Deng, W. (2013). The littoral zone in the Three Gorges Reservoir, China: Challenges and opportunities. *Environmental Science and Pollution Research*, *20*(10), 7092–7102. <https://doi.org/10.1007/s11356-012-1404-0>
- Zhang, Z., Wu, Q., Hou, M., Tai, B., & An, Y. (2021). Permafrost change in Northeast China in the 1950s–2010s. *Advances in Climate Change Research*, *12*(1), 18–28. <https://doi.org/10.1016/j.accre.2021.01.006>
- Zhao, G., & Gao, H. (2018). Automatic correction of contaminated images for assessment of reservoir surface area dynamics. *Geophysical Research Letters*, *45*(12), 6092–6099. <https://doi.org/10.1029/2018GL078343>
- Zhao, G., Li, Y., Zhou, L., & Gao, H. (2022). Evaporative water loss of 1.42 million global lakes. *Nature Communications*, *13*(1), 3686. <https://doi.org/10.1038/s41467-022-31125-6>
- Zhao, S., Zeng, R., Zhang, H., Meng, X., Zhang, Z., Meng, X., et al. (2022). Impact of water level fluctuations on landslide deformation at Longyangxia Reservoir, Qinghai Province, China. *Remote Sensing*, *14*(1), 212. <https://doi.org/10.3390/rs14010212>
- Zhu, J., Song, C., Wang, J., & Ke, L. (2020). China's inland water dynamics: The significance of water body types. *Proceedings of the National Academy of Sciences*, *117*(25), 13876–13878. <https://doi.org/10.1073/pnas.2005584117>

References From the Supporting Information

- Chen, M., Dong, Z., Jia, W., Ni, X., & Yao, H. (2019). Multi-objective joint optimal operation of reservoir system and analysis of objectives competition mechanism: A case study in the Upper Reach of the Yangtze River. *Water*, *11*(12), 2542. <https://doi.org/10.3390/w11122542>
- Ding, W., Wei, G., & Zhou, H. (2023). Improving flood resilience through optimal reservoir operation. *Journal of Hydrology*, *620*, 129494. <https://doi.org/10.1016/j.jhydrol.2023.129494>
- Guo, J., Zhang, C., Zheng, G., Xue, J., & Zhang, L. (2018). The establishment of season-specific eutrophication assessment standards for a water-supply reservoir located in Northeast China based on chlorophyll-a levels. *Ecological Indicators*, *85*, 11–20. <https://doi.org/10.1016/j.ecolind.2017.09.056>
- Guo, Y., Fang, G., Xu, Y.-P., Tian, X., & Xie, J. (2021). Responses of hydropower generation and sustainability to changes in reservoir policy, climate and land use under uncertainty: A case study of Xinanjiang Reservoir in China. *Journal of Cleaner Production*, *281*, 124609. <https://doi.org/10.1016/j.jclepro.2020.124609>
- Li, J.-Q., Zhang, Y.-S., Ji, C.-M., Wang, A.-J., & Lund, J. R. (2013). Large-scale hydropower system optimization using dynamic programming and object-oriented programming: The case of the Northeast China Power Grid. *Water Science and Technology*, *68*(11), 2458–2467. <https://doi.org/10.2166/wst.2013.528>
- Liu, Z., & He, X. (2023). Balancing-oriented hydropower operation makes the clean energy transition more affordable and simultaneously boosts water security. *Nature Water*, *1*(9), 778–789. <https://doi.org/10.1038/s44221-023-00126-0>
- Wang, G., Wu, B., & Wang, Z.-Y. (2005). Sedimentation problems and management strategies of Sanmenxia Reservoir, Yellow River, China. *Water Resources Research*, *41*(9), 09417. <https://doi.org/10.1029/2004WR003919>
- Wang, S., Fu, B., Piao, S., Lü, Y., Ciais, P., Feng, X., & Wang, Y. (2016). Reduced sediment transport in the Yellow River due to anthropogenic changes. *Nature Geoscience*, *9*(1), 38–41. <https://doi.org/10.1038/ngeo2602>
- Wu, Y., & Chen, J. (2013). Estimating irrigation water demand using an improved method and optimizing reservoir operation for water supply and hydropower generation: A case study of the Xinfengjiang reservoir in southern China. *Agricultural Water Management*, *116*, 110–121. <https://doi.org/10.1016/j.agwat.2012.10.016>
- Yi, S., Song, C., Wang, Q., Wang, L., Heki, K., & Sun, W. (2017). The potential of GRACE gravimetry to detect the heavy rainfall-induced impoundment of a small reservoir in the upper Yellow River. *Water Resources Research*, *53*(8), 6562–6578. <https://doi.org/10.1002/2017WR020793>